Fragmentation Cross Sections of 290 and 400 MeV/nucleon ^{12}C Beams on Elemental Targets

C. Zeitlin, S. Guetersloh, L. Heilbronn, and J. Miller
*Lawrence Berkeley National Laboratory, Berkeley, CA 94720**

A. Fukumura, Y. Iwata, and T. Murakami
National Institute of Radiological Sciences, Chiba, Japan
(Dated: May 8, 2007)

Charge-changing and fragment production cross sections at 0° have been obtained for interactions of 290 MeV/nucleon and 400 MeV/nucleon carbon beams with C, CH_2, Al, Cu, Sn, and Pb targets. These beams are relevant to cancer therapy, space radiation, and the production of radioactive beams. We compare to previously published results using C and CH_2 targets at similar beam energies. Due to ambiguities arising from the presence of multiple fragments on many events, previous publications have reported only cross sections for B and Be fragments. In this work we have extracted cross sections for all fragment species, using data obtained at three distinct values of angular acceptance, supplemented by data taken with the detector stack placed off the beam axis. A simulation of the experiment with the PHITS Monte Carlo code shows fair agreement with the data obtained with the large acceptance detectors, but agreement is poor at small acceptance. The measured cross sections are also compared to the predictions of the one-dimensional cross section models EPAX2 and NUCFRG2; the latter is presently used in NASA's space radiation transport calculations. Though PHITS and NUCFRG2 reproduce the charge-changing cross sections with reasonable accuracy, none of the models is able to accurately predict the fragment cross sections for all fragment species and target materials.

PACS numbers: 25.75.-q, 25.70.Mn, 25.60.Dz, 24.10.Lx, 98.70.Sa

I. INTRODUCTION

Carbon ions are currently used for radiotherapy at several major facilities [1, 2]. They are also a significant component of the Galactic Cosmic Radiation [3], and as such are a source of dose to astronauts on long-duration space missions [4]. In heavy charged particle radiotherapy, fragmentation of the primary ions has the undesirable effect of reducing dose localization, since some fragments have ranges greater than that of the primary, and also because their trajectories may be sufficiently perturbed compared to that of the incident ion that they deposit a non-negligible dose outside the volume of tissue being treated. Detailed knowledge of carbon fragmentation at or near the energies of therapy beams is required to fully calculate dose to the treated site and the surrounding tissue.

In the space radiation environment, while the flux of ions in free space is reasonably well known, fragmentation in spacecraft walls and contents, including the astronauts' bodies, can lead to large uncertainties in estimates of radiation risk inside a habitat [5]. Established radiation protection practice mandates that planners err on the side of caution, so that large uncertainties in fragmentation cross sections may impose avoidable limitations on allowed mission duration, or make the cost of "adequate" shielding prohibitively high.

*Electronic address: cjzeitlin@lbl.gov

For the above reasons, an accurate and precise database of the relevant nuclear interaction cross sections is an important tool for both radiotherapy and space radiation protection. To that end, we report here two experiments performed at the Heavy Ion Medical Accelerator (HIMAC) at the Japanese National Institute for Radiological Sciences, using carbon beams at extracted energies of 290 and 400 MeV/nucleon. These beam-energy combinations are relevant for both radiotherapy and space radiation applications.

II. DETECTOR CONFIGURATIONS

A. 0° Experiment

A 0° fragmentation experiment, similar to others reported by our group [6–11] was carried out at HIMAC over two running periods, the first in February 1997 and the second in February 1998. There were small differences between the detector setups in the two runs, but the experimental methodology, described in detail in references 6 and 7, was essentially the same: silicon detectors were placed at strategically chosen points along the beamline to record the energy depositions (ΔE) of particles passing through them. Two detectors were placed upstream of the target position to provide trigger signals, and several more were located behind the target. The beam intensity must be kept low to avoid damaging the silicon detectors and to avoid event pileup, since the readout is relatively long (on the order of 200 μsec per

event). The rate was kept to about 400-500 events/sec during the spill, which was about 0.6 sec long. Data acquisition livetime was typically in the 65-80% range. In 1997, 0° data were taken with the 290 MeV/nucleon beam, and off-axis data (described below) were taken with the 400 MeV/nucleon beam. In 1998, the same two beams were used for additional 0° measurements. Target materials included carbon (2.0 and 4.0 g cm^{-2} depths), polyethylene (2.0 and 2.8 g cm^{-2}), aluminum (1.8, 3.2, and 3.5 g cm^{-2}), copper (2.8, 4.5, 5.6, and 7.2 g cm^{-2}), tin (2.2, 3.7, and 6.0 g cm^{-2}), and lead (3.6, 6.8, and 10.2 g cm^{-2}).

Figure 1 is a schematic diagram of the 0° experimental configuration in the 1998 run. (The 1997 experiment was very similar.) The first element in the stack was a 300μm thick trigger detector referred to as "TR". In the 1997 experiment, a detector with an active area of 300 mm^2 was used as TR; in 1998, this was replaced by a detector with an active area of 50 mm^2. Downstream of TR was a 5 mm thick lithium-drifted detector ("d5mmU") with an active area of about 1400 mm^2. The event trigger was defined as a coincidence of hits above threshold in these two detectors, with thresholds set to about 80% of the expected pulse height from an incident carbon ion. Targets were placed downstream of d5mmU. Surviving primaries and charged fragments exiting the target were detected using several lithium-drifted silicon detectors, most of which were 3 mm in depth (referred to as "d3mmX", with X ranging from 1 to 6). In between d3mm2 and d3mm3, a pair of position-sensitive silicon detectors (PSD's) was used to record deposited energy as well as signals proportional to the y and x coordinates (the dimensions transverse to the direction of the beam). In the 1997 experiment, no PSD's were used, and a plastic scintillator (SC1) was placed upstream of TR, providing the start signal for a time-of-flight measurement, for which SC2 (located 2.4 m downstream of d3mm6) provided the stop. A NaI counter, 12.7 cm in both diameter and depth, was placed about 10 cm behind SC2. In 1998, the plastic scintillators were configured differently: SC1 was placed downstream of d3mm6 by 0.93 m, SC2 downstream of SC1 by 2.23 m, and the NaI again about 10 cm behind SC1.

Throughout, we make frequent reference to the acceptance angles of the detectors downstream of the target. By this we mean the half-angle of the forward cone subtended by a detector, as seen from a point on the beam centerline and midway through the target. For both 1997 and 1998 configurations, d3mm1 and 2 captured particles within an acceptance of 7.3°; d3mm3 and d3mm4 had an acceptance of 3.9°; and d3mm5 and d3mm6 had an acceptance of 2.5°. (We refer to the acceptance angle of the more-downstream detector in all cases.) The measured spectra vary significantly with acceptance angle. In comparing results at different acceptances, it should be recalled that, as described by Goldhaber [12], angular distributions of projectile fragments in the laboratory frame are invariably forward peaked, with strong dependences on both the beam energy and the number of nucleons removed by interaction. All of the data reported here are at least qualitatively consistent with this picture.

Pulser calibration data were taken periodically throughout the experiments, and off-line analysis of these data yielded the scale factors that (linearly) relate pulse height to energy deposited (ΔE). While beam data were being taken, a low-rate random trigger was fired so that pedestals could be monitored. Pedestals and calibration peaks were found to be stable, drifting by at most two counts from day to day over a given run period.

B. Off-axis Experiment

In the 1997 experiment, all detectors except SC1 were moved off the beam axis and data were taken with the 400 MeV/nucleon beam. SC1 was left in place to serve as a beam counter and part of the trigger coincidence. The silicon stack was reconfigured, with the addition of four detectors of approximate depth 5 mm (d5mm1 through d5mm4), as shown schematically in Figure 2. The trigger was defined as a coincidence of hits in SC1 and d5mm1. Because the 5 mm thick detectors have more than twice the area of the 3 mm thick detectors, on many events the particle responsible for the trigger missed some or all of the 3 mm detectors. This is not a problem in the analysis discussed here, since we normalize to the solid angle of d3mm4 (the most-downstream detector used in the analysis).

Data were taken with a subset of the targets (polyethylene, carbon, copper, and lead) with the detectors placed at 5° and 10° angles with respect to the incident beam direction. The off-axis data help us resolve, on a statistical basis, some of the particle identification ambiguities that are encountered in the analysis of the 0° data. Because of the limited beam time available, statistics for these runs are modest, with about 2×10^5 events collected for each target/angle combination. In the following, we will focus only on the results obtained with a 2 g cm^{-2} carbon target; results for the other targets are similar, and a single example suffices to illustrate the important points.

III. DATA ANALYSIS

A. 0° Analysis

Since much of the data analysis methodology has been explained in previous articles, we present only a brief summary here. In the off-line analysis, we restrict the data samples to events in which a single incident carbon ion was present upstream of the target, using pulse heights in TR and d5mmU. Stringent cuts on ΔE in these two detectors are made, selecting events within about two standard deviations of the peak for a single carbon ion. These cuts define the starting sample; we then identify

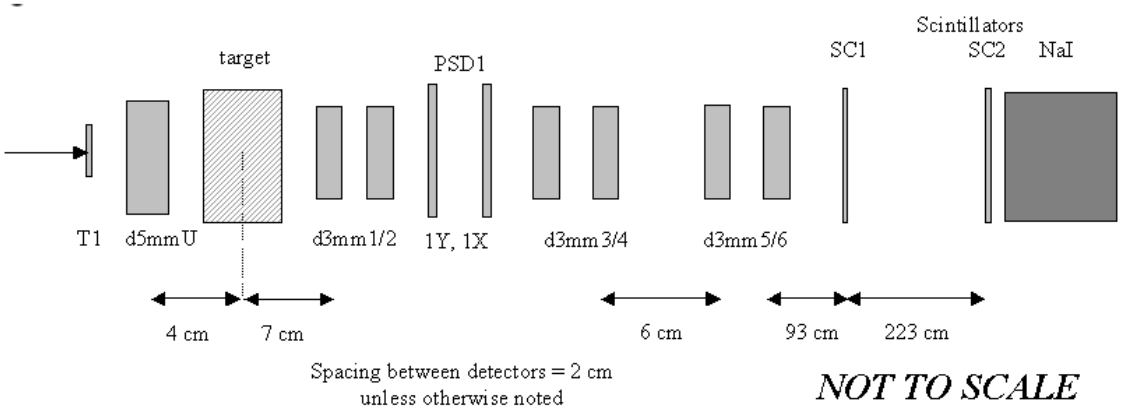

FIG. 1: Schematic diagram of the beamline configuration for the 1998 experiment. In the 1997 experiment, no position-sensitive detectors were employed, and a detector with larger area (but the same depth) was used as the trigger, or "TR," detector.

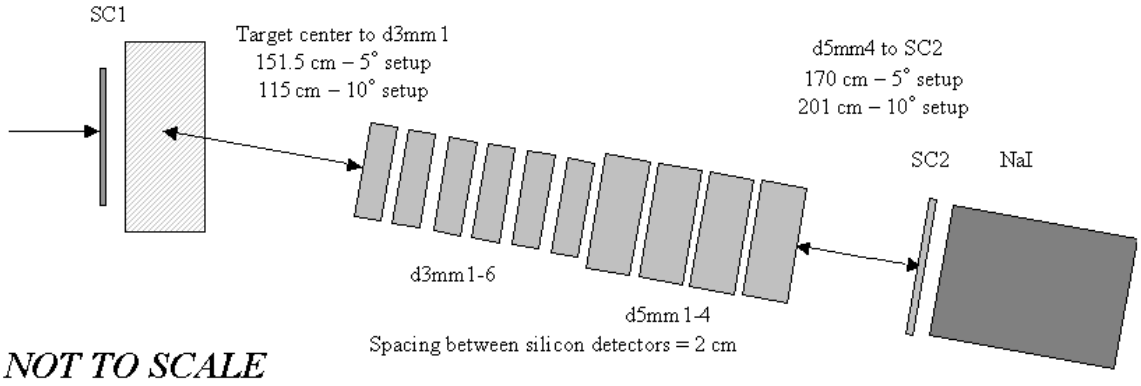

FIG. 2: Schematic diagram of the beamline configuration for the 1997 off-axis experiment. One set of runs was taken with the apparatus placed at a 5° angle with respect to the beam axis, and another set at 10°. A coincidence of hits in SC1 and d5mm1 triggered the readout.

particles downstream of the target, using scatter plots of ΔE in neighboring detectors, that is, d3mm2 vs. 1, 4 vs. 3, and 6 vs. 5 to guarantee that the samples contain only well-measured events. Graphical cuts are made in the scatter plots to remove events in which the ΔE's in neighboring detectors are not well correlated; these events are due to a variety of artifacts including particles hitting near detector edges, interacting in the silicon, etc.

To determine cross sections, events surviving the cuts are selected and a histogram of the summed ΔE in the detector pair is made. We refer to this sum as ΔE_{12} in the detector pair nearest the target, etc. With the modest target depths used here, there is always an obvious large peak corresponding to the primary carbon ions, and there is a significant peak for pedestal events. At least five other peaks are visible, but they do not simply correspond to the five ion species lighter than carbon. We return to this point below. We proceed by fitting a Gaussian distribution to the central region of the carbon peak to determine ΔE_{12}(C), i.e., the peak value of the summed ΔE's. Using only the events in this region, we make a histogram of the quantity Z_{12}, the effective charge detected, which is defined to be:

$$Z_{12} = 6\sqrt{\Delta E_{12}/\Delta E_{12}\,(C)} \qquad (1)$$

An example of the resulting charge histogram is shown in the main portion of Figure 3, for the 400 MeV/nucleon beam incident on a carbon target of 4 g cm^{-2} depth. Using the carbon peak to determine the Z scale assumes the fragment velocities are at or near that of the primary carbon; this approximation is more accurate for higher energies. The analysis procedure is repeated for the d3mm3 and 4 detector pair, and again for the d3mm5 and 6 pair, yielding histograms of Z_{34} and Z_{56}, respectively, analogous to the quantity Z_{12} defined above. As can be seen in Figure 3, treating all particles as if they are at beam

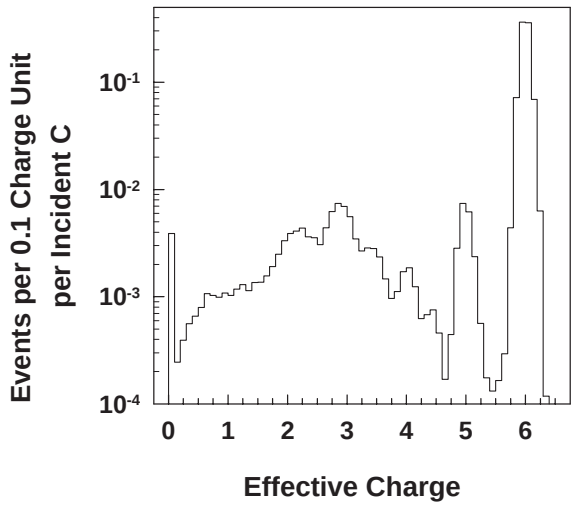

FIG. 3: Effective charge distribution in detectors d3mm1 and d3mm2, the pair nearest the target exit, for the 400 MeV/nucleon beam incident on a carbon target of depth 4.0 g cm^{-2}. These large-acceptance detectors capture a large majority of the projectile fragments, and the many possible combinations of light fragments causes the spectrum to be indistinct below charge 4. The same data set was used to produce the distributions shown in Figures 6-9 below.

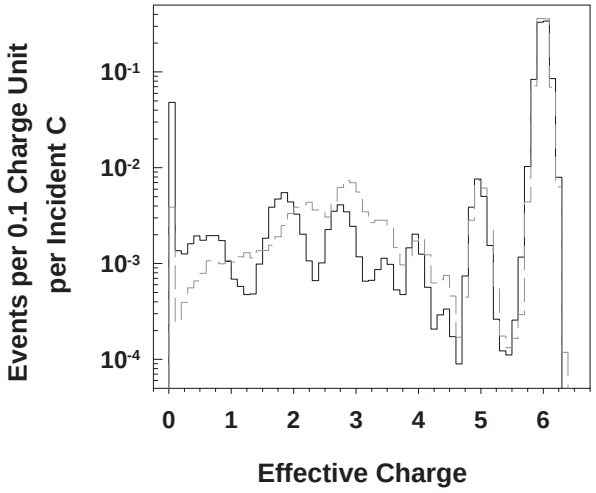

FIG. 4: Effective charge distribution in detectors d3mm5 and d3mm6, which subtend an acceptance angle of 2.5°, for the same data set as was used in Figure 3. Because many fragments, particularly the lightest, are outside this acceptance, the light fragment peaks are distinct here, in contrast with the large-acceptance spectrum. To facilitate the comparison, the histogram from Figure 3 is reproduced here with a grey line.

velocity works well for the B and Be fragments, as peaks are seen at Z_{12} of 5 and 4. Other reasonably clear peaks are seen near $Z_{12} = 3$, just above 2, and between 4 and 5. Less distinct, but invariably present in these data, is the peak about midway between charges 3 and 4. The region from Z_{12} of 0 to about 1.8 does not contain obvious peaks. The peaks at the non-integer values of Z are discussed further in Section V below.

An additional cut is made in the analyses of the downstream detector data: a scatter plot is made with ΔE in the most-downstream detector of the pair plotted against ΔE in d3mm1, the first detector downstream of the target. In these plots (e.g., ΔE in d3mm6 on the ordinate, ΔE in d3mm1 on the abcissa), obvious vertical bands of events appear which are due to the fragmentation of carbon ions in the detector stack. Events in these bands are removed, as they constitute a significant background to the fragments of interest, i.e., those produced in the target. These plots also show several horizontal bands of events with multiple fragments in d3mm1 but only a single fragment in d3mm3/4 or d3mm5/6. (An example of this type of plot and cut contour, for 600 MeV/nucleon ^{20}Ne beam data, is shown in Figure 5 of Ref. [9].)

Deeper in the detector stack, where the angular acceptance is smaller, the non-integer-value peaks in the charge histograms are less populated. This is due to the fragment transverse momentum (p_T) distributions, which broaden with decreasing fragment mass. As angular acceptance decreases, so too does the probability for detecting multiple fragments. As a consequence, the spectra from downstream detectors are noticeably different from those obtained at large acceptance. Figure 4 shows a histogram of Z_{56} (acceptance angle of 2.5°) obtained using the same data set as in Figure 3. The peaks below charge 4 are much clearer than those seen with the larger-acceptance (7.3°) detectors, and a peak near charge 1 is evident here where there was none in Figure 4. The charge 1 and 2 peaks are shifted to slightly less than their nominal values; this is due to the breakdown of the method of scaling ΔE to charge, since, deep in the stack, the light fragments have higher velocities than do surviving carbon ions and heavier fragments. It is also notable that the peak at $Z \approx 2.8$ is shifted to the left (by about 0.1 charge unit relative to Figure 3) and is somewhat narrower (FWHM of 0.47 charge units compared to 0.60 charge units).

B. Off-axis Data Analysis

Analysis of the off-axis data is straightforward. Although a more sophisticated analysis is possible, for present purposes we simply require well-correlated ΔE signals in the first four detectors in the stack (d3mm1-4), and we use these signals to identify particles by species. The energy depositions are summed and scaled to Z as in the 0° analysis, but with the scale factor chosen so that the Z = 2 peak comes out at exactly 2.0. A histogram of the 5° data is shown in Figure 5, with the 10° obtained with the same 2 g cm^{-2} C target superimposed. Both histograms contain a large fraction of events

(not shown in the figure) in which no particle hit the 3 mm detectors, since the trigger depended on a larger-area detector, as explained above. Ignoring those, we see in the 5° data, peaks for all ion species between H and C, and no evidence of peaks corresponding to multiple fragments detected in coincidence. Significantly, the charge 3 peak falls exactly at 3.0, unlike that seen in the 0° data, where it was both broad and offset so that it appeared to be somewhere between 2.8 (corresponding to two He fragments) and 3.0. The sparsely-populated peaks for charges 4, 5, and 6 in Figure 5 are at values slightly above the exact integer value corresponding to the charge, presumably because these ions are on average at slightly lower velocities than the He fragments used to scale the spectra. The charge 1 peak falls slightly below 1.0, since those fragments are on average at higher velocity than the He fragments used to calibrate the scale. In the 10° data, clear peaks are seen for charges 1 and 2, with comparatively more events in the high-ΔE tails, corresponding to fragments with lower velocities than those in the peaks. Near charge 3, a shoulder is seen on the tail of the charge 2 distribution, and at charge 4, there appears to be a very small peak. A single event is seen near charge 5, and none near charge 6. The integrated counts per species, *N(Z)*, are normalized to the total number of primary carbon ions recorded in the beam counting scintillator, N_{pri} and the corresponding number obtained in the target-out runs is subtracted. (Both target-in and target-out data are corrected for livetime.) The differential cross section is then given by:

$$\frac{d\sigma}{d\Omega} = \frac{(N\,(Z)/LN_{pri} - N_{to}\,(Z)/L_{to}N_{pri-to})}{\Delta\Omega}\frac{A_{tgt}}{\rho x N_A} \quad (2)$$

where the subscript *"to"* refers to target-out data, L is the livetime, N_A is Avogadro's number, $\Delta\Omega$ is the solid angle subtended by d3mm4 as seen from the center of the target, and the other variables refer to the target.

To determine $d\sigma/d\Omega$ for each species, we count only those fragments that are at or near beam velocity, i.e., projectile fragments. These populate the peak regions, particularly in the 5° spectra. Accordingly, in all cases but one, we fit Gaussian distributions to the central bins of each charge peak and determine the numbers of events in the peaks from the fit parameters. The one exception to this procedure was for charge 3 in the 10° spectrum. Since there appears to be a large high-end tail of slower He fragments that reaches to and beyond Z = 3, we fit that region with the sum of an exponential (to approximately account for the slow He) and a Gaussian (to account for the actual charge 3 events).

IV. EVENT CATEGORIES IN THE 0° DATA

Once the histograms of Z_{12}, Z_{34}, and Z_{56} have been made, the numbers of events in the different categories are determined. Because the C and B peaks are large and well separated, we simply count numbers of events directly from the histograms. We also count the number in the pedestal, the (loosely defined) charge 1 events – those in between the He peak and the pedestal peak – and the charge 2 events directly from the histograms.

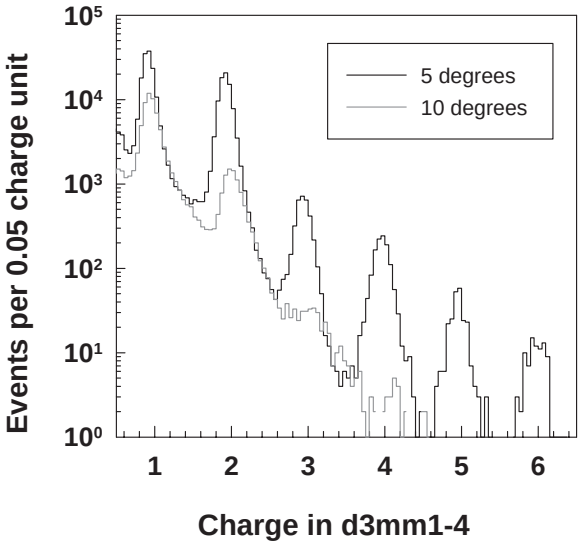

FIG. 5: Charge distributions obtained in the off-axis experiment with a 2 g cm^{-2} C target and the 400 MeV/nucleon beam. The energy deposited in detectors d3mm1-4 was summed and scaled so that the He peak is centered at 2.0.

The remaining five peaks in the Z plots are identified as follows. The peak near Z = 2 (typically around 2.25 in the Z histograms) corresponds to a single He fragment, probably in coincidence with one or more protons. The peak near Z = 3, typically centered slightly below 3, is broad because it contains both events with a single Li fragment and events with two He fragments in coincidence (Z ≈ 2.8). The peak near Z = 3.5 is due to three He fragments in coincidence or one Li fragment and one He fragment. The peak at charge 4 is due to Be, possibly with one or two protons; and the peak at Z = 4.4 is due to Be + He. The peaks below Be overlap one another substantially, particularly in the large-acceptance spectra.

To obtain estimates of the numbers of events in each category for each histogram, we performed a simultaneous fit of six Gaussian distributions using PAW [13]. Five of the six peaks that are fit are those described just above; the sixth Gaussian is fit to the B peak, even though we also directly count those events, because doing so constrains the width of the Be + He peak and gives a consistency check. The inset histogram in Figure 3 shows a typical fit result. The procedure begins by fitting six individual Gaussians to the central bins in the peaks. The bins to be fit must be chosen with care, avoiding bins where the neighboring peak contributes significantly. The pa-

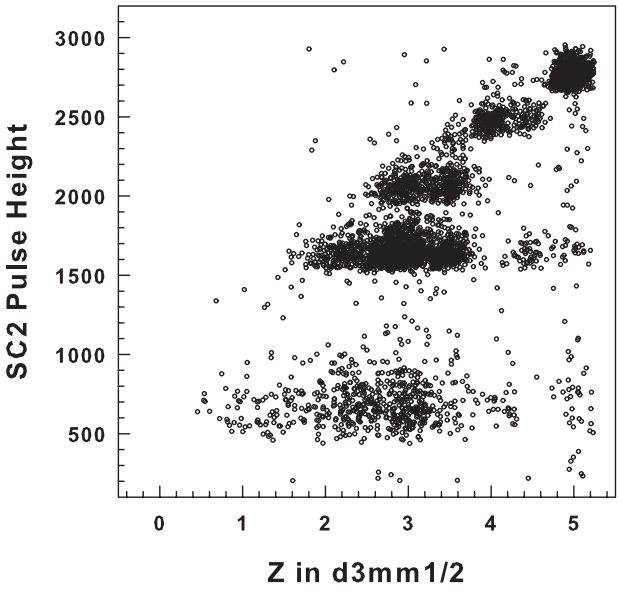

FIG. 6: From the 0° experiment, pulse height in the downstream plastic scintillator SC2, plotted against Z_{eff} in detectors d3mm1/2. The locations of event clusters suggest that the peaks near 3.5 and 3 are dominated by events with three and two helium fragments, respectively.

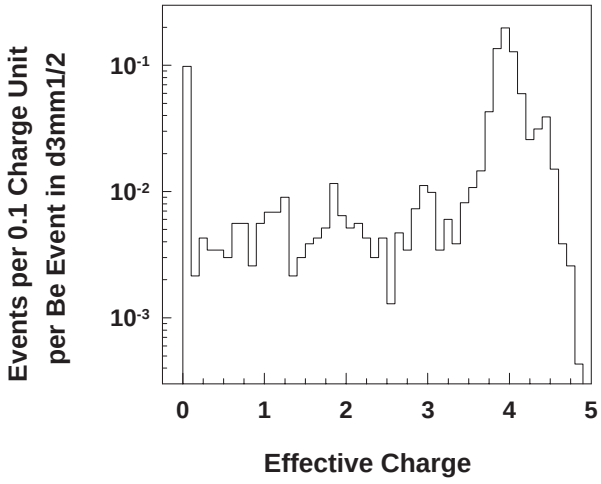

FIG. 7: Effective charge distribution in the d3mm5,6 pair, for events in which a Be (or Be+He) signal was recorded in d3mm1,2. In about 72% of the events, the Be fragment remained within the acceptance. A small fraction (about 4%) of events are consistent with a Li fragment in d3mm5,6; these could be due to a Be fragment undergoing a charge-changing reaction in the detector stack, or they could be due to events in which the apparent Be signal in d3mm1,2 is a result of two Li fragments detected in coincidence.

rameters obtained for the singly fit Gaussians are used as the starting values for the simultaneous six-Gaussian fit. The number of events in a given peak is determined from the fit parameters; uncertainties are obtained by summing in quadrature the relative errors on amplitude and width. This significantly overestimates the uncertainties because the fit parameters are negatively correlated, so that the reported errors are conservatively large.

A. Multiple-Fragment Events

Several peaks in the 0° spectra are attributed to the detection of multiple fragments in coincidence, as per the above. The scatter plot shown in Figure 6, in which pulse height in SC2 is plotted against Z_{12}, taken together with the results of the off-axis data analysis, provides the basis of these interpretations. Events in which the primary carbon survived beyond the target have been removed from the plot, as have those in which the SC2 pulse height was consistent with its pedestal value.

1. Events with a Leading Be Fragment

Among the peaks due to multiple fragments, the easiest to interpret is the peak near effective charge of 4.4. This peak is dominated by events in which a Be fragment is detected in coincidence with a He fragment. (Since ^{8}Be is unstable, these events cannot consist of ^{8}Be + ^{4}He, and instead must be due to ^{7}Be and ^{4}He with an undetected neutron, or ^{9}Be and ^{3}He.) In Figure 6, the region with $Z_{12} = 4.4$ contains two distinct clusters of events, one with a pulse height in SC2 of ≈ 1700 channels, corresponding to a He fragment, the other at about channel number 2400, consistent with the detection of only the Be fragment. Though in principle this peak could contain a contribution from events with two Li fragments in coincidence, which would be expected to yield $Z_{12} \approx 4.2$, no cluster of events is seen in the region with SC2 pulse height around channel 2100, where such events would appear. We can further explore these events using the downstream silicon detectors. Figure 7 shows a histogram of Z_{56} for events in the $Z_{12} \approx 4.4$ peak. The dominant peak remains consistent with Be + He (containing 49% of the events), with a smaller but significant peak at $Z_{56} = 4$ (with 29% of the events), and a small peak just below Z_{56} of 2. (The shift of fragment peaks to lower-than-nominal values in d3mm5,6 is due to the velocity differences between fragment species discussed above.) The absence of a significant peak at 3 in the Z_{56} histogram affirms that these events are dominantly Be + He.

2. Events Consistent with Three He Fragments

The peak in the vicinity of $Z_{12} \approx 3.5$ is similarly dominated by events in which three He (possibly all ^{4}He) ions

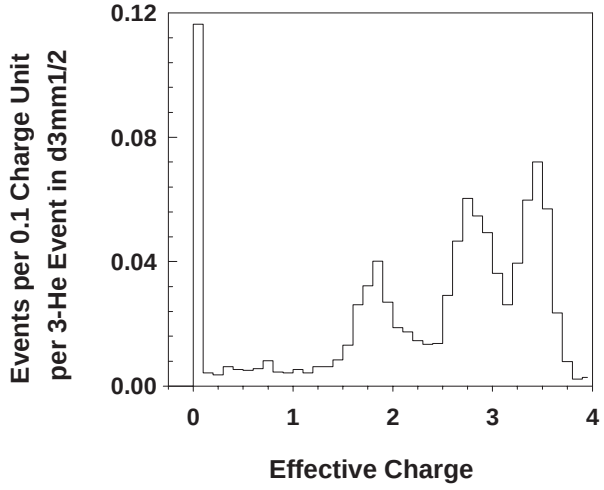

FIG. 8: Effective charge distribution in the d3mm5,6 pair, for events in which the signal in d3mm1,2 was consistent with three He fragments in coincidence. In about 30% of the events, all three He fragments remain within the acceptance; a roughly equal number of events are consistent with two He fragments remaining in the acceptance, and 20% of the events contain only a single He fragment within the smaller acceptance. In most of the other events, only pedestals were recored in d3mm5,6. (Note, a linear scale is used here and in Figure 9, whereas the similar figures - 3, 4, and 7 - employ a logarithmic scale.)

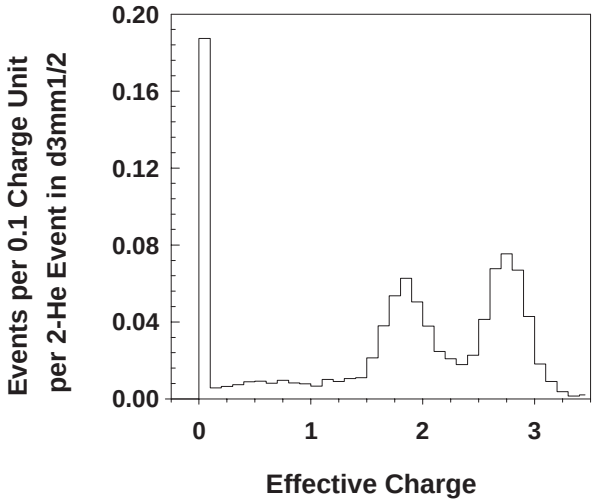

FIG. 9: Effective charge distribution in the d3mm5,6 pair, for events in which the signal in d3mm1,2 was consistent with a single Li fragment, or two He fragments in coincidence. In 37% of the events, the d3mm5,6 signal is consistent with two He fragments remaining in the acceptance, while 30% of the events contain only a single He fragment within the smaller acceptance, and in 20% of the events only pedestals were recored in d3mm5,6.

are detected in coincidence. This is expected to be a favored mode of ^{12}C fragmentation, based on the very small mass difference between the primary nucleus and the fragments[14]. (Some such events may arise in the reaction ^{12}C $\rightarrow^{8}$Be + ^{4}He $\rightarrow^{4}$He + ^{4}He + ^{4}He.) Events with one Li and one He fragment would also appear in this peak. In Figure 6, in the region of the plot with $Z_{12} \approx 3.5$, three clusters of events are seen: the lower two, at SC2 pulse heights of ≈ 1700 and 2100, are heavily populated and correspond to the detection of one and two He fragments, respectively, while the third cluster, at SC2 pulse height of ≈ 2350, is sparsely populated and corresponds to all three He fragments hitting SC2. We note too that for events with a single He fragment in SC2 (pulse height 1700), there are three heavily-populated clusters as one looks along the Z_{12} axis, centered (approximately) at 2.2, 2.8, and 3.5 in Z_{12}. Figure 8 shows Z_{56} for events in the $Z_{12} \approx 3.5$ peak; as was the case for SC2, there are obvious peaks in this plot corresponding to a single He fragment ($Z_{56} \approx 1.8$, 21% of events), two He fragments or one Li fragment ($Z_{56} \approx 2.8$, 31%), and three He fragments ($Z_{56} \approx 3.4$, 28%), as well as a large peak of pedestal events (12%).

3. Events with One Li Fragment or Two He Fragments

The peak just below $Z_{12} = 3$ in Figure 3 contains events with a Li fragment and events with two He fragments, but it is dominated by the latter, which gives $Z_{12} \approx 2.8$. The two populations cannot be separated from $Z_{12} = 3$ based simply on ΔE, due to the intrinsic widths of the fragment velocity distributions, which result in overlapping Z_{12} distributions. (Even a detector with very high spatial resolution might not allow clean separation of Li fragments from pairs of ^{4}He arising from ^{8}Be decay, which are expected to have very little separation of their trajectories due to the very small Q of the decay.) Again examining the relevant region in Figure 6, three distinct clusters of events can be seen in the $Z_{12} \approx 3$ region, corresponding to SC2 signals consistent with a proton (pulse height ≈ channel number 600), a single He ion (≈ channel 1700), and an ambiguous cluster around channel number 2100. The latter is ambiguous because it contains events with a single Li fragment and events with two He fragments. This cluster is less populated than the one corresponding to a single He fragment in SC2. We can make a quantitative assessment using the spectrum shown in Figure 9, which is the Z_{56} distribution for the $Z_{12} \approx 3$ peak. Approximately 36% of the events remain in the Li/He + He peak, while 33% appear in the single-He peak, and 19% of the events appear as pedestals in d3mm5,6.

B. Acceptance Calculations

A straightforward calculation of acceptance using Goldhaber's formulation (Gaussian distributions in each momentum coordinate in a Cartesian frame), with σ_0 set to 90 MeV/c, and allowing for Coulomb scattering in the target, was performed. This initial value of σ_0 is based on previously reported data [15] (in particular, see Figure 1 therein), which show a large scatter in the value reported for low fragment masses. The model predicts that the standard deviation of the angular distribution for ^{4}He fragments is 3.3°, resulting in a 57% probability of individual ^{4}He fragments being within both the d3mm1/2 and the d3mm5/6 acceptances, and (making the unphysical assumption that there are no correlations between fragments) a $0.57^3 = 0.19$ probability that all three remain inside the d3mm5/6 acceptance. This does not apply to ^{4}He fragments arising from ^{8}Be decays; if ^{8}Be were stable, the model predicts that 87% of such fragments would be within the d3mm5/6 acceptance. Applying that probability to two He fragments, and assuming a 57% acceptance for the third, results in a total probability of 50% for all three being detected in d3mm5/6. Similarly, in the case of a ^{7}Li fragment produced with a ^{4}He fragment, there would be a 46% probability that both remained within the d3mm5/6 acceptance. The predictions of this simple model for the various outcomes are summarized in Table 1; the uncertainties in the model probabilities, given in the columns labeled "Calc. 1", reflect ±10 MeV/c changes in σ_0. It can be seen that the ^{8}Be and ^{7}Li cases give very similar results, but do not come close to matching the data. The probabilities for three independently-produced ^{4}He fragments also fail to match the data, but the value corresponding to $Z_{56} \approx 3.5$ comes considerably closer to the data than do the two other cases.

The calculations suggest that, as one might expect, the observed spectra are an admixture of the three combinations of fragments. We can come reasonably close to reproducing the data by (arbitrarily) assuming various mixtures of the three, but we find that adjusting σ_0 to 110-120 MeV/c generally yields the best agreement. Table 1 therefore includes, in the columns labeled "Calc. 2," the calculated acceptance probabilities with $\sigma_0 = 120$ MeV/c. (Tripathi *et al.* have pointed out that there are two parts to σ_0, the intrinsic and dynamical, which are added in quadrature to obtain the total. To the extent that these data measure σ_0, the result corresponds to the total width, which must be larger than the intrinsic width.) Since the ^{8}Be contribution actually corresponds to a pair of ^{4}He fragments, the result obtained with an equal mixture of all three combinations is consistent with 2/3 of the $Z_{12} \approx 3.5$ events containing two ^{4}He ions. However, this is far from a unique solution, and other mixtures cannot be ruled out. It is worth noting that it is not possible to adjust σ_0 such that either the (Li + He) or (^{8}Be + He) combinations can explain the data; both yield fractions of $Z_{56} \approx 3.5$ and 2.8 that are larger than the fractions in the data, and a fraction of $Z_{56} \approx 2$ that is less than the fraction in the data. Simply put, to match the data, the model requires a significant contribution from the three-He-fragments category, and also points to a larger than expected value of σ_0.

Applying the simple acceptance model to the $Z_{12} \approx 2.8$ case, the probability for a ^{7}Li fragment to be inside the d3mm5/6 acceptance is 80%, assuming $\sigma_0 = 90$ MeV/c. The probability for an event with two ^{4}He fragments in d3mm1/2 to be seen as $Z_{56} \approx 2.8$ is 33%, to be seen as $Z_{56} = 2$ is 49%, and to be seen as a pedestal event is 18%. Since fragmentation of Li into He in the stack has a low probability (< 5% in traversing d3mm1 through d3mm4), events with a Li fragment in d3mm1/2 will typically populate one of two regions in d3mm5/6, $Z \approx 3$, or pedestal. However, a relatively large fraction of the $Z \approx 3$ events in d3mm1/2 are seen as $Z \approx 2$ in d3mm5/6, which strongly suggests that these events are predominantly due to two He fragments inside the d3mm1/2 acceptance. Again, one can reproduce the data with various combinations of the possible initial states and different values of σ_0, and - as above - no unique solution emerges. However, all plausible solutions require that a majority of the events correspond to (He + He) in d3mm1/2, and are consistent with σ_0 in the range 110 to 120 MeV/c.

It does not appear possible to extract more precise or more quantitative information from the data with this type of analysis. The essential difficulty is the similarity in energy depositions arising from a single Li fragment or two He fragments, owing in part to the finite widths of the velocity distributions. At higher beam energies, fragment velocity widths would be narrower, and it might be possible to separate the two contributions. However, with the 0° data discussed so far, we are limited, and so we examine other data for clarification.

C. Particle Identification Using the NaI

It is possible to use the signals from the NaI counter to distinguish events with a single Li fragment from those with two He fragments. Although the counter is much larger in diameter (12.7 cm) than the silicon detectors, it was placed far downstream, about 3.5 m from the target center, so that its front face subtends a small acceptance cone of 0.8°. There are two issues with the NaI counter that limit its usefulness. First, because its acceptance was small, it recorded only a small (highly A-dependent) fraction of the total number of particles that exited the target. Second, even for stopping particles, in many cases the range is comparable to the nuclear interaction length, meaning that many ions will undergo charge-changing interactions in the crystal; the result - even for a monoenergetic pure beam of a single ion species - are ΔE distributions with long tails to the low end. Third, the intrinsic resolution of NaI is not as good as silicon. And, finally, even if the resolution of the NaI were perfect, the mix of ions and energies that reach it in an experiment such

TABLE I: For the 400 MeV/nucleon beam and carbon target, the measured and calculated probabilities for detecting a particular Z_{eff} in the d3mm5/6 detector pair, given an event consistent with three He fragments in d3mm1/2. Details of the calculations are explained in the text.

Z_{eff} at 2.5°	P(Data)	If due to	Calc. 1	Calc. 2	If due to	Calc. 1	Calc. 2	If due to	Calc. 1	Calc. 2
3.5	0.28	3 ^{4}He	0.19±0.05	0.12	^{7}Li+^{4}He	0.46±0.06	0.33	^{8}Be+^{4}He	0.50±0.06	0.37
≈ 3.0	0.31	2 ^{4}He	0.42±0.02	0.37	^{7}Li	0.33±0.01	0.34	^{8}Be	0.36±0.01	0.38
2.0	0.21	^{4}He	0.31±0.04	0.38	^{4}He	0.12±0.03	0.17	^{4}He	0.08±0.02	0.13
Ped.	0.12		0.07±0.02	0.13		0.09±0.03	0.17		0.06±0.03	0.13

as this produces spectra that can be difficult to interpret. For example, for typical target depths used here, the energy deposited in the NaI by a ^{11}B fragment is very close to that deposited by a ^{12}C primary, both of which stop in the detector. One might expect a difference of 8% based on the difference in masses, but the C loses more energy in traversing the detectors and air gaps upstream of the NaI, resulting in nearly equal ΔE in the NaI. Similarly, there are some cases (depending on the target depth) in which lower-mass isotopes (^{6}Li and ^{7}Be) deposit slightly more energy in the NaI than do the higher-mass isotopes of the same species (^{7}Li and ^{9}Be). This is because the lower-mass isotopes stop in the NaI, while the higher-mass isotopes do not. For both species, the energy deposited by the two isotopes is expected to be nearly equal. Thus, on the whole, particle identification using ΔE in the NaI alone is problematic. Nonetheless, and in spite of the very limited statistics, the NaI data are useful for the specific question we wish to resolve - species identification of He vs. Li fragments. The primary reason is the very small acceptance, which greatly reduces the number of multiple-fragment events seen. Also, at these energies, in traversing such a substantial depth of material, Li fragments lose energy more rapidly than do He fragments, and consequently the ratio of deposited energies is slightly greater than the $\approx(3/2)^2$ that is seen in the silicon detectors; we expect little overlap of the Li and two-He ΔE distributions, even in those rare instances when both He fragments are recorded in the NaI.

Using data from the same 400 MeV/nucleon C beam on the 4 g cm^{-2} C target as in the above discussion, we show in Figure 10 a histogram of ΔE in the NaI for events in which the primary carbon underwent a charge-changing interaction in the target. The figure shows the region of the histogram corresponding to charge 3 and below. Over 90% of the entries in the histogram are pedestals, indicating that no charged particle hit the NaI. The vertical scale has been adjusted to suppress the pedestal peak so that the rest of the spectrum is more visible. The ΔE scale was determined from the location of the C peak and the calculated value of ΔE for this target. In the figure, apart from the pedestal peak, two other peaks are obvious, one near 75 MeV, the other near 390 MeV. These correspond to H and He, respectively. The ΔE spectrum predicted by our simplistic one-dimensional Monte Carlo simulation[16] is also shown. The Monte Carlo spectrum has been normalized so that its He peak bin contains the same number of events as the peak bin in the data. There is a slight offset between the two He peaks, and another offset (in the opposite direction) in the vicinity of the small Li peak near 1000 MeV. The Monte Carlo, which relies on NUCFRG2 [17] for nuclear cross sections and the Bethe-Bloch equation for energy loss calculations, does a fair job of reproducing the data, although there are relatively more Li fragments in the Monte Carlo than in the data. The Monte Carlo spectrum contains most (about 60%) of the Li in the range of ΔE from about 900 to 1100 MeV in the NaI. About 60% of the He will deposit between 350 and 450 MeV in the NaI.

Integrating the numbers of events in the He peak and in the region expected to be populated by Li fragments, we find about five times more He fragments than Li. Our acceptance model calculation predicts approximately 50% greater acceptance for Li than for He, depending on the choice of σ_0 and the isotopes considered. This implies that the number of He fragments is about 7.5 times greater than the number of Li fragments. As will be seen in the following section, this estimate is highly consistent with the estimate obtained using the off-axis data.

V. OFF-AXIS RESULTS

Although the scatter plot in Figure 6 and the histograms in Figures 7 through 10 support the interpretations offered in the previous section, the off-axis data may be more definitive, particularly since there do not appear to be any multiple-fragment events in the spectra. Differential cross sections for the 400 MeV/nucleon beam incident on the 2 g cm^{-2} carbon target are given in Table 2 for charges 1 to 5 at 5° and for charges 1 to 3 at 10°. A 3% systematic uncertainty has been added in quadrature to the statistical error on each cross section. For charges 1 and 2, the systematic uncertainty dominates; for heavier fragments, statistical errors dominate.

For charges 1 to 4, two data points are available and we can fit them (with no degrees of freedom) to an exponential in θ^2 in order to determine the width (σ_θ) of the presumed Gaussian angular distributions. The results are shown in Table 2, along with predictions from the simple angular distribution model discussed above.

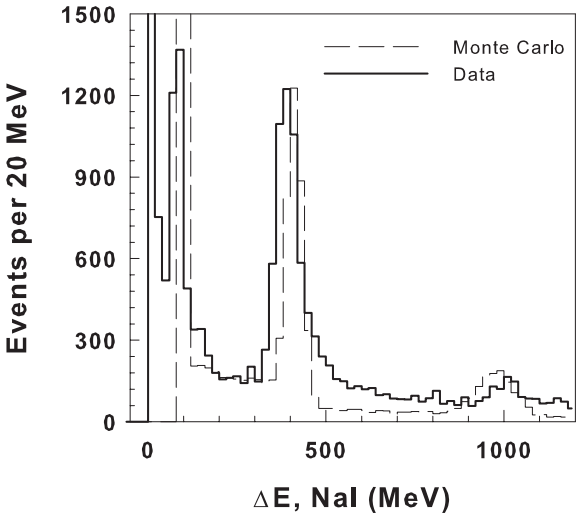

FIG. 10: Deposited energy spectrum in the NaI with the 400 MeV/nucleon beam and targets of depth 3-4 g cm^{-2}. Aside from the large peak of pedestal events, clear peaks corresponding to H and He fragments are seen, as well as a small, broad peak of Li fragments near 1000 MeV deposited.

TABLE II: Differential cross sections obtained in the off-axis experiment with the 400 MeV/nucleon beam and 2.0 g cm^{-2} carbon target.

Z	dσ/dΩ, 5°, b sr^{-1}	dσ/dΩ, 10°, b sr^{-1}	σ_θ fit, degrees	σ_θ model, degrees
1	7.63±0.23	4.17±0.16	7.9±0.4	7.8±0.9 (A=1)
				5.2±0.6 (A=2)
2	4.22±0.13	0.61±0.04	4.4±0.2	4.1±0.4 (A=3)
				3.3±0.4 (A=4)
3	0.20±0.01	0.011±0.005	3.6±0.7	2.4±0.2 (A=6)
				2.0±0.2 (A=7)
4	0.054±0.005	0.003±0.002	3.5+1.4–2.8	2.0±0.2 (A=7)
				1.4±0.1 (A=9)

The uncertainties in the model come from varying the σ_0 parameter ± 10 MeV/c from the central value of 90 MeV/c. The measured widths are, except for hydrogen, somewhat larger than the model predicts, although the uncertainties for Li and Be are so large as to render those results essentially meaningless.

We find that dσ/dΩ for Z = 1 at 5° and 10° reported here (7.6 ± 0.2 mb sr^{-1} and 4.2 ± 0.2 mb sr^{-1}, respectively) for the 400 MeV/nucleon beam, are quite close to the corresponding neutron production cross sections (integrated over energy) reported by Iwata *et al.* using the 290 MeV/nucleon ^{12}C beam at HIMAC. (See Figure 10a.) One would expect that the neutron cross section as measured might be somewhat larger than the proton cross section, since it is integrated over a larger range of energy and contains contributions from neutrons evaporated from the target. However at forward angles, the d$^2\sigma$/dΩdE is dominated by projectile-like neutrons, making this a reasonable comparison. Fragments from interactions of the 290 MeV/nucleon are less forward-focused than those produced in the 400 MeV/nucleon beam, which may compensate for the difference in energy ranges spanned by the integrations. (Note that the 400 MeV/nucleon neutron cross sections at forward angles reported in Ref. [18] are well below both the QMD model to which the data are compared - which fits their other data well - and the 290 MeV/nucleon ^{12}C beam data shown in the same article. We think the comparison to the 290 MeV/nucleon neutron data is more reliable.)

For present purposes, the off-axis data are of particular interest since they may give insight into the Li and He cross sections, which, as discussed above, are difficult to disentangle in the 0° data. The 10° results are not helpful in determining the Li abundance at 0°, since the uncertainty in the differential cross section is so large, so the following discussion is limited to the 5° measurement. There, the dσ / dΩ for He is seen in Table 2 to be about 20 times larger than that for Li. Our simple model of fragment angular distributions predicts that the Li differential cross section is extremely sensitive to the isotope being considered (^{6}Li vs. ^{7}Li), and to the value of σ_0 chosen for the calculation. The NUCFRG2[17] and EPAX2 models [19] used here, and described below, both predict that about 60% of the Li fragments produced are ^{6}Li. The 0° analysis above suggests that a comparatively large value for σ_0, in the range of 110-120 MeV/c, is appropriate for these data. Taking the low end of the range, and assuming a 60:40 mix of ^{6}Li to ^{7}Li, the acceptance model predicts that the cross section for Li will, at 5°, have fallen to a value of about 18% of its value at 0°. Similarly, assuming that ^{4}He dominates and again using σ_0 = 110 MeV/c, the model predicts that the He cross section falls to about 47% of its value at 0°. Roughly speaking, we can estimate that the differences in angular distributions account for a factor of 2 to 3 difference in the measured cross sections, leading us to conclude that C + C interactions at this energy yield approximately seven to ten times as much He as Li. The analysis above using the NaI in the 0° data yielded an estimate of 7.5 times more He than Li, quite consistent with this result.

The off-axis results also show that charge 1 particles (probably dominantly protons) are copiously produced. The 0° spectra tend to obscure this fact since the presence of one or more protons has, in most cases, little effect on Z_{eff}. The cross sections in Table 2 can be integrated (assuming a Gaussian form for the angular distributions, and using the measured values of σ_θ), with the result that the total yield of protons is about double that of helium.

VI. MODELS

The NUCFRG2 [17] and EPAX2 [19] cross section models, and the PHITS (Particle and Heavy Ion Transport System) Monte Carlo simulation [20, 21] were

used to compare measured data with calculations of charge changing and fragment production cross sections. NUCFRG2 performs a one-dimensional transport calculation, using an approach based on finding an analytic solution to the Boltzmann equation in the straight-ahead approximation. The underlying model of fragmentation is an abrasion-ablation formulation. The output of the code is, for each combination of beam ion, energy, and target, a list of cross sections for all isotopes that can be generated in the interaction; no geometry is specified. Cross sections for H and He fragments in NUCFRG2 are multiplicity weighted, making comparisons to these data (in which no multiplicities are measured) difficult. There is no straightforward way to use NUCFRG2 as a standalone program to simulate the complexity of the charge histograms. EPAX2 output is similar to that of NUCFRG2, and it too is a one-dimensional code. Of the three models, only PHITS allows (with some effort) a realistic comparison to the experiment.

A. PHITS Simulation

1. Geometry Model

In the simulations of carbon beams performed here, we did not use the exact experimental geometry, as was done elsewhere [22]. Instead, the simulations performed for this comparison were designed to yield cross sections based on effective charge detected, closely corresponding to the data. The differences between the simulated geometry and the actual experiment warrant discussion. First, since corrections to the experimental data account for, among other things, interactions in the detectors themselves, silicon was not used as a detector material in the model. In the simulation, the detectors were set up as void regions to eliminate fragmentation in the detector stack, and no such correction to the Monte Carlo cross sections was needed. Particle identification (Z, A, and kinetic energy) was obtained directly by scoring forward-going particles in each region of interest, defined to correspond to the three experimental acceptance angles. Having direct information on particle charge, systematic errors in counting were eliminated and the reported errors are entirely statistical. Finally, as PHITS does not simulate the artifacts associated with the detectors, it was not necessary to require detector-pair correlations in the simulated data, as was done in the analysis of the experimental data.

In the initial simulations, it was quickly determined that target fragments were being produced in the interactions, transported to, and registered in, the void regions corresponding to the detectors. This was due to the fact that particles leaving the target in these simulations were being transported in vacuum, whereas in the actual experiments, there is an air gap between the target and the first detector. The air gap has two major effects, the most important of which is that it stops low-energy target fragments and ionization electrons that emerge from the target before they reach the first detector. A less important effect of the air gap is the fragmentation of a very small fraction of the ions leaving the target. This is corrected in the data with the target-out subtraction, which also accounts for other "dead" materials on the beamline. Changing from vacuum to air in the simulation for the gap between the target and the first detector effectively removed most of the very low energy particles that exit the target. We do not perform a target-out correction in the simulation, but the effect on the cross section results is negligible (about 0.03% of carbon ions would be expected to fragment in 7 cm of air, and the distance from the target exit to d3mm1 is always less than this).

Unlike the experiment, only a single thickness, 1 g cm^{-2} was chosen for each target, eliminating the need to correct for secondary and higher interactions in the target. A hydrogen target was run directly in the simulation, and results were found to be consistent with those obtained using a carbon/polyethylene subtraction as in the data. For each target, 10^6 primaries were simulated to ensure sufficient statistics in the lower-charge fragment peaks.

2. Reconstruction of Simulated Events

An important distinction between this work and past simulations [23] is that here the events were reconstructed in a manner analogous to how they were measured in the experiment. Most important was the combining of multiple fragments produced when primaries interacted. Inelastic nuclear collisions typically produce multiple forward-going fragments with velocities close to that of the projectile ion. Any such fragments within the acceptance angle subtended by a detector will strike the detector, for practical purposes simultaneously, and are recorded as a single pulse. To recreate this aspect of the measurements, it was essential to turn off particle biasing, which has been used to reduce calculation times in other work. When run in full analog mode, PHITS allows the user to output information requested for every particle tracked using the "dump" command. Each tracked particle that crosses the region of interest is output to a text file, line by line in order of occurrence. All fragments produced by the same collision, if crossing the boundary describing a detector, are therefore listed sequentially, including their charge and mass. Analysis of this output would be a true "track" analysis, but would not be directly comparable to the analysis of experimental data, which is an "event" analysis. (For further elucidation of this point, see the Appendix in Ref. [24].)

In analyzing the simulated data, we read in all sequential fragments occurring in the output file and created a single event when certain criteria were met. If the particle read in was a surviving primary beam ion, it was written to a new file and the next particle was read in. When a particle was found that had a charge less than that of the

beam it was banked in memory and the next particle was read in, continuing until the next beam ion was found. All sequential fragments stored in memory before finding the next beam ion were then processed further. If the sum of Z of all fragments was less than that of the beam, a single event was written with an effective Z equal to the square root of the sum of squares of all Z's stored. Since it is possible, however, that two or more consecutive beam ions could undergo a nuclear interaction, adding the charge of all sequential fragments could exceed beam Z. In this case, an effective Z was determined for the first set of particles summing to the beam charge and a single event was written. This process was repeated until all fragments were accounted for. Since neutron stripping does not change the charge of a projectile these events were written back as beam ions. The final 'event' output was counted based on effective charge, in analogy with the data, and cross sections determined.

3. Results of Event Reconstruction

Figure 11 shows the result of creating events by this method for a 290 MeV/nucleon ^{12}C beam on an aluminum target. If a true track analysis were performed, the peaks would occur only at integer values of charge, as shown in Figure 11a. Here, however, and as discussed in Section V above, the combinations of particles leading to an event create non-integer peaks. In the experiment we record ΔE, and convert to effective charge, but in the simulation it is trivial to obtain the effective Z directly. In counting the events by effective charge in the data, variations due to possible proton combinatorics are not resolvable; the simulated data were handled analogously. The result is shown in Figure 11b. We note that in Figure 11a, the total number of He fragments produced is 10-15 times greater than the number of Li fragments. This is a somewhat larger ratio than is suggested by the data, which suggest there is 7 to 10 times more He than Li.

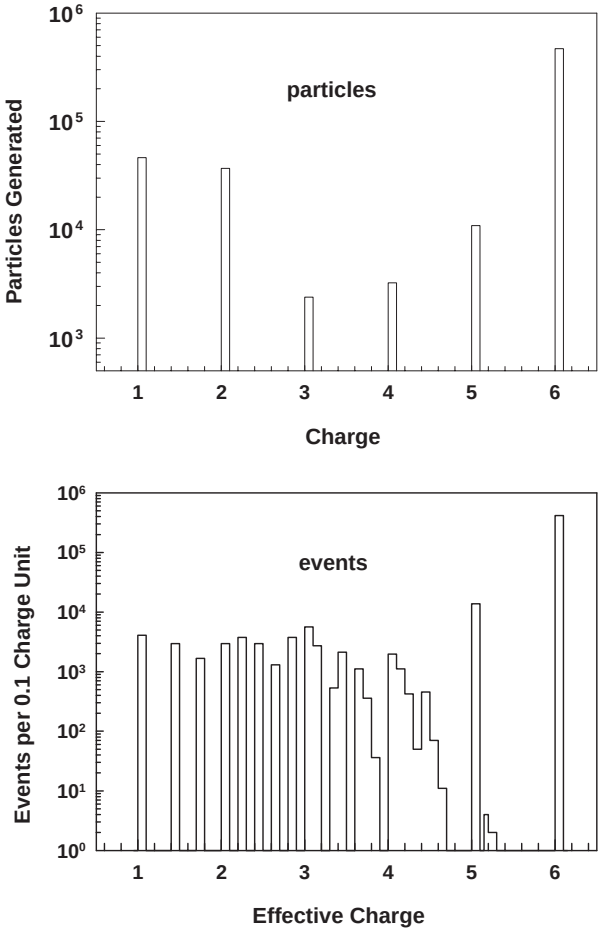

FIG. 11: Above, Figure 11a shows a histogram of particle charges produced by PHITS for a 290 MeV/nucleon carbon beam incident on an aluminum target. Below, Figure 11b shows the charge distribution after combining the fragment charges, as in the measurements. These are referred to as "track" and "event" analyses, respectively.

VII. MEASURED CHARGE-CHANGING CROSS SECTIONS

A. Methodology

The numbers of events in each category in the charge histograms, determined by the methods described above, are used to determine the charge-changing and fragment production cross sections. Several selection cuts and corrections are needed. These have been explained in detail in Refs. 8 to 11, and account for the following effects:

1) Events lost due to charge-changing nuclear interactions in the detectors;

2) Interactions in materials other than the target and silicon stack (air gaps, detector dead layers); and

3) Incomplete charge collection.

Because the data from detectors d3mm1-2 require the smallest corrections, we use those results for the charge-changing cross sections, σ_{cc}.

The data analysis depends on graphical cuts made interactively using the CERN library software package PAW, and as a result, the cross sections are prone to variations arising from the small degree of subjectivity involved in drawing cut contours. Efforts were made to perform analysis as consistently as possible on all data sets, and, in extracting results we take into account the systematic errors arising from the method. The relative uncertainties on the fragment cross sections are generally much larger than those associated with the charge-changing cross sections. The uncertainties on the fragment cross sections, particularly at large acceptance where peaks are indistinct, are the propagated relative errors from the multiple-Gaussian fits described above.

For each target material, we have two or three runs using different depths. As in our previous work, the RMS deviation in the values of the cross sections for each material is typically 1-3%, which is substantially greater than accounted for by the statistical errors alone. We attribute the spread to systematic errors in the data analysis procedure, and incorporate these errors into the subsequent analysis as follows. For each material, the RMS deviation of the σ_{cc}'s is calculated and divided by the weighted average cross section. This relative error is then added in quadrature to the statistical error for each run, and the weighted average and total error are re-calculated. As an example of the process, we consider the cross sections obtained from three separate measurements of the 290 MeV/nucleon beam on aluminum targets. If only statistical errors were considered, the weighted average cross section would be 1057 ± 1 mb, and the χ^2 for combining the data would be absurdly large, 349 for 2 degrees of freedom. Including the RMS deviation of 1.8% as a systematic uncertainty in each measurement, the reweighted cross section becomes 1052 ± 11 mb, with a much more reasonable χ^2 of 3.9 for 2 degrees of freedom. In the few cases where the RMS deviations of a set of σ_{cc} values are less than 1.5% of the average, we assign a 1.5% error, which reflects the variations observed in results obtained by independent analysis of the same data sets by different individuals.

B. Charge-Changing Cross Section Results and Model Comparisons

Table 3 shows the measured and calculated charge-changing cross sections for both beams and all target materials, along with model calculations. The data are presented graphically in Figure 12. The first calculation uses the NUCFRG2 code [17], which agrees with the measured cross section to within 15%. The next is a simple geometric cross section calculation based on the Bradt-Peters [25] formulation with parameters determined by Chen *et al.* [26]. Using the values as per Chen *et al.* ($r_0 = 1.35$, $b = 0.83$), the calculations are within 14% of the data in all cases. The second version of Bradt-Peters we present uses adjusted parameters ($r_0 = 1.29$, $b = 0.86$) and comes within 3% for all measurements except 290 MeV/nucleon C on Cu, which is within 5%. (This is the same value of b we found in Ref. 9 fitting this same form to ^{20}Ne beam data at 600 MeV/nucleon, but a 4% smaller value of r_0.) The results of the PHITS Monte Carlo simulations are within 7% of the data except for 290 MeV/nucleon C on H. Charge-changing cross sections were also calculated by summing up fragment cross sections produced by the energy-independent EPAX2 model. These can be seen to deviate widely from the data. Finally, charge-changing cross sections for H and C targets were reported by Webber *et al.* [27] at energies almost identical to those in the present experiment. These are also shown in Table 3, and are seen to agree with the present measurement to better than 13% in the four comparable cases.

In the last section of Table 3, we show the ratios of the 400 and 290 MeV/nucleon charge-changing cross sections for the data and the calculations. In the data, the ratios of the σ_{cc}'s at the two energies are, for the most part, consistent with 1.0. A slight decrease at the higher energy is seen for heavy targets. PHITS reproduces this trend, but predicts an increase for the hydrogen target that is not seen. NUCFRG2 predicts that the cross sections increase slightly with increasing energy, which is also not seen.

VIII. FRAGMENT PRODUCTION CROSS SECTIONS

The formalism for obtaining the charge-changing cross section is easily extended to determine the (partial) cross sections for the production of individual fragment types. Here, we do not attempt to identify isotopes of a given species, nor, for reasons outlined above, do we attempt to separate events with a Li fragment from those with two detected He fragments.

Once we have the corrected fractions for the various fragment species and the charge-changing cross section, the cross section for a fragment of charge Z is given by:

$$\sigma_Z = \frac{f_Z}{\sum\limits_{Z<Z_{prim}} f_Z} \sigma_{cc} \tag{3}$$

where the sum in the denominator runs over all fragments. It is trivial to show that the sum of all fragment cross sections defined in this way equals the charge-changing cross section. The cross sections are corrected for the effects of secondary and higher interactions in the target, as discussed elsewhere 8.

A. Results

Tables 4 through 6 show the results for the 290 MeV/nucleon beam, and Tables 7 through 9 show the 400 MeV/nucleon results. All are uncorrected for acceptance effects. Tables 4 and 7 show results for 7.3° acceptance (d3mm1-2), 5 and 8 are for 3.9° (d3mm3-4), and 6 and 9 are for 2.5° (d3mm5-6). Although we can distinguish between the Be + He and the Be-only in the spectra, the measured cross sections tend to have large errors. We cannot, for the most part, distinguish between combinations with differing proton multiplicities when heavier fragments are detected. Protons contribute little to the effective charge of a measured event, but do increase the widths of the distributions. And although Li fragments and events with two He fragments (ignoring permutations involving protons) can be distinguished in the PHITS calculation, they are not distinguishable in the data. Thus, for the comparisons, these events are

TABLE III: Charge-changing cross sections for the two beam energies and all targets.

Charge-changing cross sections (mb)	H target	C target	Al target	Cu target	Sn target	Pb target
^{12}C 290 MeV/nucleon						
This work	158 ± 9	706 ± 7	1052 ± 11	1625 ± 18	2069 ± 18	2795 ± 15
NUCFRG2	175	795	1123	1639	2220	2883
Bradt-Peters(1)	—	805	1139	1707	2329	3114
Bradt-Peters(2)	—	723	1026	1541	2107	2820
PHITS	137 ± 1	689 ± 1	1042 ± 1	1601 ± 2	2182 ± 3	2949 ± 4
Weber et al.	158 ± 3	658 ± 7				
^{12}C 400 MeV/nucleon						
This work	160 ± 11	713 ± 11	1011 ± 9	1557 ± 10	2035 ± 21	2745 ± 45
NUCFRG2	184	806	1137	1656	2243	2913
Bradt-Peters(1)	—	805	1139	1707	2329	3114
Bradt-Peters(2)	—	723	1026	1541	2107	2820
PHITS	150 ± 1	681 ± 1	1032 ± 1	1581 ± 2	2162 ± 3	2948 ± 4
EPAX2	99	240	317	426	527	635
Weber et al.	181 ± 4	672 ± 7				
σ_{cc}(400)/σ_{cc}(290)						
This work	1.01	1.01	0.96	0.96	0.98	0.98
NUCFRG2	1.05	1.05	1.01	1.01	1.01	1.01
PHITS	1.09	0.99	0.99	0.99	0.99	1.00
Weber et al.	1.15	1.02				

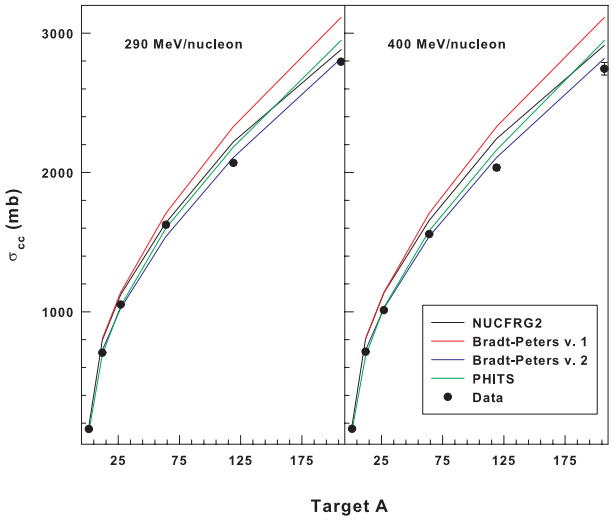

FIG. 12: Comparison of charge-changing cross sections between the data (black diamonds), PHITS calculations (green lines), NUCFRG2 (black lines), and two versions of the Bradt-Peters model (red and blue lines). The plot on the left is for the 290 MeV/nucleon beam, on the right for 400 MeV/nucleon.

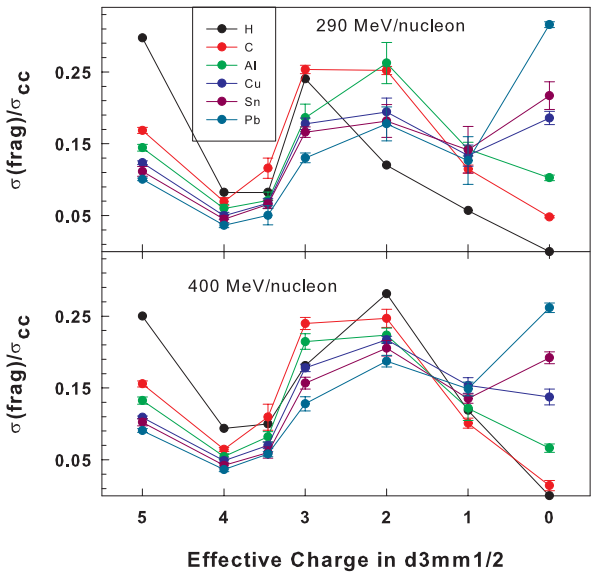

FIG. 13: Fragment cross sections normalized to the charge-changing cross section for that material, for the 290 MeV/nucleon beam (above) and the 400 MeV/nucleon beam (below).

all reported under the Z ≈ 3 category for both data and PHITS results. The entries in the table for NUCFRG2 and EPAX2 in this category are predictions for Li fragments only and are shown alongside our estimated Li cross sections, as discussed in more detail below. The single He and proton categories also include contributions from multiple-fragment events; the labels refer to the leading fragment. We also show cross sections for pedestal events, which presumably are events where all fragments are outside the acceptance.

Using the results in Tables 4 and 7, we can make a multiplicity-weighted estimate of the cross section for helium fragment production. Since we cannot say whether the Z ≈ 3 category consists of mostly events with single

Li or two He fragments, we proceed as follows: we add the cross sections for (Be + He), three He, Li/two He, and He, with weights of 1, 3, 1, and 1, respectively. The uncertainty is set equal to half the Li/two He cross section, typically about 15% of the total. This assumes that 50% ± 25% of the Li/two He events are due to events with two He fragments (hence the overall weight of 1). The uncertainty is chosen to be conservatively large, so that, at the two-sigma level, it covers all possibilities. The results are shown near the bottom in Tables 4 and 7. Dividing these totals by the charge-changing cross section for each target gives an estimate of the average He multiplicity per fragmentation event; the results are all in the range from about 0.8 for the low-A targets (H through Al) to about 0.55 for the higher-A targets.

Since the estimates of Li yield using both NaI spectra and the off-axis data are consistent with the He:Li ratio being in the range of 7 to 10, we have estimated the Li cross sections by scaling the estimated total He production cross sections. We take the scaling factor to be 0.12 with an uncertainty of ± 0.02; the results are shown in the last rows of Tables 4 and 7.

In Figure 13, the fragment cross sections in Tables 4 and 7 have been divided by the corresponding charge-changing cross sections, and the data for all targets plotted as color-coded series. (To keep the plot readable, the large error bars for the hydrogen target data are omitted.) For fragment charges 5 and 4, the fractions go in sequence with the highest values for the H target and lowest for Pb; the order is nearly preserved for Z ≈ 3.5. For pedestals (shown as effective charge 0 in the figure), the order is exactly reversed. There are a few other features in Figure 12 that bear discussion. First, for the 290 MeV/nucleon beam and the aluminum target, it appears that effective charge ≈ 3 is enhanced, and charge 2 depleted. This may be an artifact of the multiple-Gaussian fits to the spectra, in which the parameters for neighboring distributions are negatively correlated with one another. A shift of about 10% of the $Z_{12} = 2$ events (corresponding to a one-sigma change) into the $Z_{12} \approx 3$ category would produce a result much more like that seen in the 400 MeV/nucleon data. Similarly, for hydrogen, there is an apparent difference between the two energies for $Z_{12} = 2$ and $Z_{12} \approx 3$ cross sections. However, the 290 MeV/nucleon data for this target have particularly large uncertainties, and, as can be seen by comparing the H results in Tables 4 and 7, the differences are actually insignificant.

Some trends in the cross sections are readily apparent and are qualitatively as expected. Among these are the following: all fragment production cross sections increase with increasing target mass; detected cross sections for all fragment categories except protons and pedestals monotonically decrease with decreasing acceptance (and for the Cu, Sn, and Pb targets, this applies to protons as well); and pedestal cross sections increase with decreasing acceptance for all targets. These features are seen at both beam energies, as well as in the PHITS simulation.

B. Dependence on Energy, Target, and Acceptance Angle

Comparing the 7.3° acceptance (d3mm1,2) results in Tables 4 and 7, few significant differences are seen between the two beam energies. Only two consistent trends are apparent, for the largest and smallest charge changes: First, the B production cross sections ($\Delta Z = 1$) are larger at 290 MeV/nucleon than at 400 MeV/nucleon. Second, pedestal cross sections are also larger at 290 MeV/nucleon, with the insignificant exception of the hydrogen target. For other categories, no clear patterns emerge when comparing the two tables. The decrease of the $\Delta Z = 1$ cross section in going from 290 to 400 MeV/nucleon is also seen clearly in recently-published ^{28}Si data [11] for lower-mass targets. The larger pedestal cross sections at lower energy are likely due to the comparatively broader (less forward-focused) fragment angular distributions at the lower energy. While one might expect more collisions to completely fragment the projectile at the higher energy, any such increase is apparently outweighed by the focusing effect.

The cross sections for pedestals are strongly dependent on target mass. The cross sections are zero for H targets, but as a fraction of the charge-changing cross section, they increase monotonically with target mass, reaching 32% for Pb. In general, interactions with higher-mass target nuclei are more likely to produce larger charge changes. This effect is evident in Figure 13.

To further sort out dependences on acceptance, beam energy and target mass, we have computed the ratios of cross sections in the smallest acceptance detectors (2.5°) to those in the largest acceptance pair (7.3°) Results for both beam energies are presented in Table 10. Results for hydrogen have been omitted owing to excessively large uncertainties in the ratios. For the other targets, several notable trends are apparent. First, for a given target, the ratios are larger for the unambiguous single-fragment categories (Z = 2,4,5) than for the categories we interpret as being partly or entirely composed of multiple-fragment events (Z ≈ 3, 3 He, Be + He). Second, in all categories except single-He and protons, the ratio for 400 MeV/nucleon data is greater than the corresponding ratio for 290 MeV/nucleon; this is due to the greater forward focusing at 400 MeV/nucleon. Third, with few exceptions, the ratios show little or no dependence on target mass. We return to this point below.

It is also apparent in Table 10 that the smallest ratios are for the three-He-fragments category and the Be + He category. This is not surprising, considering that in order to be detected in d3mm5-6 all of the fragments must be contained in a forward cone of less than 2.5°. If one fragment is emitted at a larger angle, the event as recorded in d3mm5-6 would be in a different category. This has the effect of increasing the ratios for the lowest

TABLE IV: Fragment cross sections for the 290 MeV/nucleon beam using the large-acceptance detectors (7.3° acceptance).

Z_{eff}		H target	C target	Al target	Cu target	Sn target	Pb target
5	This work	47 ± 2	119 ± 3	152 ± 5	201 ± 4	231 ± 14	281 ± 5
	NUCFRG2	73	148	166	192	217	243
	EPAX2	26	63	84	113	139	168
	PHITS	75 ± 1	72 ± 1	87 ± 2	104 ± 3	117 ± 6	115 ± 9
4.4 (Be+He)	This work	6 ± 1	16 ± 2	19 ± 2	20 ± 3	37 ± 6	24 ± 4
	PHITS	2 ± 1	7 ± 1	9 ± 1	11 ± 1	17 ± 2	16 ± 3
4.0 (Be only)	This work	8 ± 3	33 ± 3	43 ± 6	60 ± 7	55 ± 8	77 ± 8
	PHITS	14 ± 1	30 ± 1	35 ± 1	43 ± 2	60 ± 4	62 ± 7
Leading Be	This work	13 ± 3	49 ± 4	63 ± 6	81 ± 8	93 ± 10	102 ± 9
(sum)	NUCFRG2	54	51	57	66	74	83
	EPAX2	24	58	76	102	126	153
	PHITS	16 ± 1	37 ± 1	44 ± 2	54 ± 2	77 ± 5	78 ± 7
3.5 (3 He or	This work	13 ± 3	82 ± 10	75 ± 12	109 ±11	136 ±12	141 ± 37
Li+He)	PHITS	9 ± 1	56 ± 1	99± 2	139 ± 3	164 ± 7	146 ± 10
≈ 3 (2 He	This work	38 ± 7	179 ± 4	196 ± 20	289 ± 13	344 ± 15	364 ± 19
or 1 Li)	PHITS	20 ± 1	101 ± 1	107 ± 2	122 ± 3	135 ± 6	197± 12
≈ 2	This work	19 ± 17	178 ± 4	276 ± 30	316 ± 31	376 ± 47	497 ± 66
	EPAX2	18	44	58	78	96	116
	PHITS	12 ± 1	227± 2	291 ± 4	375 ± 5	473 ± 11	588 ± 20
1	This work	9 ± 30	81 ± 4	150 ± 10	217 ± 24	293 ± 67	354 ± 93
	EPAX2	15	35	47	63	78	94
	PHITS	7 ± 1	124 ± 1	247 ± 4	378 ± 5	526 ± 12	713 ± 22
Pedestals	This work	0 ± 3	34 ± 1	108 ± 4	302 ± 15	449 ± 40	883 ± 11
	PHITS	0 ± 0	71 ± 1	168 ± 3	429 ± 6	691 ± 14	1112 ± 28
All He (estimated)	This work	102 ± 19	619 ± 90	716 ± 98	952 ± 145	1167 ± 172	1308 ± 182
	NUCFRG2	216	186	197	222	248	275
σ(He)/σ_{cc}	This work	0.65 ± 0.12	0.88 ± 0.13	0.68 ± 0.09	0.59 ± 0.09	0.56 ± 0.08	0.47 ± 0.07
Li (estimated)	This work	12 ± 2	68 ± 12	86 ± 14	114 ± 19	140 ± 23	157 ± 26
	NUCFRG	26	92	103	120	136	152
	EPAX2	16	40	53	71	87	106

TABLE V: For the 290 MeV/nucleon beam, fragment cross sections as measured with an acceptance angle of 3.9°.

Z_{eff}		H target	C target	Al target	Cu target	Sn target	Pb target
5	This work	44 ± 3	116 ± 5	146 ± 4	191 ± 4	209 ± 14	255 ± 8
	PHITS	74 ± 1	56 ± 1	52 ± 2	51 ± 2	60 ± 4	59 ± 6
4.4 (Be+He)	This work	5 ± 3	10 ± 2	4 ± 2	15 ± 3	18 ± 4	16 ± 6
	PHITS	2 ± 1	3 ± 1	2 ± 1	2 ± 1	3 ± 1	3 ± 1
4.0 (Be only)	This work	7 ± 2	30 ± 3	38 ± 4	43 ± 6	60 ± 6	64 ± 6
	PHITS	14 ± 1	20 ± 1	19 ± 1	17 ± 1	19 ± 2	31 ± 5
Leading Be	This work	11 ± 4	41 ± 2	44 ± 4	61 ± 6	78 ± 7	78 ± 10
(sum)	PHITS	15 ± 1	22 ± 1	21 ± 1	19± 1	21 ± 2	33 ± 5
3.5 (3 He or	This work	12 ± 2	43 ± 4	56 ± 3	60 ± 8	73 ± 6	72 ± 6
Li+He)	PHITS	7 ± 1	21 ± 1	20 ± 1	20 ± 1	28± 3	26 ± 4
≈ 3 (2 He	This work	17 ± 4	124 ± 3	148 ± 8	177 ± 8	228 ± 12	227 ±10
or 1 Li)	PHITS	12 ± 1	33± 1	29 ± 1	25 ± 1	31 ± 3	44 ± 5
≈ 2	This work	29 ± 2	152 ± 2	194 ± 7	243 ± 8	272 ± 12	335 ± 8
	PHITS	19 ± 1	187 ± 2	223 ± 3	265 ± 4	315 ± 9	374 ± 16
1	This work	12 ± 3	91 ± 5	150 ± 6	195 ± 24	191 ± 12	329 ± 89
	PHITS	3 ± 1	107 ± 1	162 ± 3	214 ± 4	289 ± 9	372 ± 16
Pedestals	This work	12 ± 6	155 ± 16	292 ± 29	650 ± 65	926 ± 93	1441 ± 144
	PHITS	6 ± 1	465 ± 2	536± 5	1007 ± 8	1437 ± 19	2040 ± 37

TABLE VI: For the 290 MeV/nucleon beam, fragment cross sections as measured with an acceptance angle of 2.5°.

Z_{eff}		H target	C target	Al target	Cu target	Sn target	Pb target
5	This work	41 ± 4	109 ± 5	130 ± 5	173 ± 3	191 ± 17	223 ± 7
	PHITS	73 ± 1	21 ± 1	14 ± 1	15 ± 1	17 ± 2	23 ± 4
4.4 (Be+He)	This work	3 ± 2	8 ± 3	4 ± 1	7 ± 2	10 ± 4	5 ± 3
	PHITS	1 ± 1	1 ± 1	0 ± 1	0 ± 1	1 ± 1	1 ± 1
4.0 (Be only)	This work	7 ± 2	25 ± 3	38 ± 4	42 ± 4	51 ± 5	60 ± 6
	PHITS	13 ± 1	9 ± 1	8 ± 1	5 ± 1	5 ± 1	11 ± 3
Leading Be	This work	10 ± 3	34 ± 2	43 ± 3	50 ± 4	62 ± 6	66 ± 7
(sum)	PHITS	14 ± 1	9 ± 1	7 ± 1	5 ± 1	6 ± 1	12 ± 3
3.5 (3 He or	This work	10 ± 2	23 ± 1	27 ± 2	29 ± 5	37 ± 7	25 ± 7
Li+He)	PHITS	4 ± 1	3 ± 1	2 ± 1	2 ± 1	2 ± 1	3 ± 1
≈ 3 (2 He	This work	8 ± 1	80 ± 2	101 ± 4	117 ± 5	134 ± 9	147 ± 8
or 1 Li)	PHITS	16 ± 1	12 ±1	9 ± 1	8 ± 1	11 ± 2	17 ± 3
≈ 2	This work	26 ± 3	124 ± 4	164 ± 4	187 ± 7	220 ± 8	275 ± 11
	PHITS	12 ± 1	112 ± 1	122 ± 2	118 ± 3	173 ± 7	175 ± 11
1	This work	26 ± 3	87 ± 4	151 ± 11	158 ± 31	129 ± 6	204 ± 116
	PHITS	3 ± 1	67 ± 1	90 ± 2	116 ± 3	143 ± 6	206 ± 12
Pedestals	This work	47 ± 19	261 ± 26	405 ± 41	799 ± 80	1244 ± 124	1861 ± 200
	PHITS	16 ± 1	465 ± 2	799 ± 6	1336 ± 9	1830 ± 21	2515 ± 41

TABLE VII: For the 400 MeV/nucleon beam, fragment cross sections as measured with an acceptance angle of 7.3°.

Z_{eff}		H target	C target	Al target	Cu target	Sn target	Pb target
5	This work	40 ± 4	111 ± 3	134 ± 5	170 ± 3	208 ± 10	249 ± 7
	NUCFRG2	76	146	164	190	217	246
	EPAX2	26	63	84	113	139	168
	PHITS	75 ± 1	73 ± 1	86 ± 2	107 ± 3	115 ± 6	153 ± 10
4.4	This work	4 ± 2	12 ± 2	13 ± 1	20 ± 2	23 ± 3	31 ± 4
(Be+He)	PHITS	1 ± 1	7 ± 1	9 ± 1	12 ± 1	16 ± 2	26 ± 4
4.0	This work	11 ± 2	34 ± 3	42 ± 4	56 ± 6	63 ± 6	69 ± 7
(Be only)	PHITS	15 ± 1	27 ± 1	36 ± 1	41 ± 2	52 ± 4	54 ± 6
Leading Be	This work	15 ± 3	46 ± 2	55 ± 4	76 ± 6	86 ± 7	100 ± 8
(sum)	NUCFRG2	54	50	56	65	73	82
	EPAX2	24	58	76	102	126	153
	PHITS	17 ± 1	34 ± 1	45 ± 1	52 ± 2	68 ± 4	79 ± 7
3.5 (3xHe or	This work	16 ± 2	78 ± 13	83 ± 7	109 ± 7	122 ± 16	159 ±10
Li+He)	PHITS	8 ± 1	48 ± 1	91 ± 2	152 ± 3	192 ± 7	196 ± 12
≈ 3 (2 He	This work	29 ± 10	171 ± 6	217 ± 11	277 ± 8	319 ± 17	351 ± 27
or 1 Li)	PHITS	25 ± 1	110 ± 1	129 ± 2	156 ± 3	192 ± 7	240 ± 13
≈ 2	This work	45 ± 10	176 ± 9	226 ± 10	338 ± 8	418 ± 22	514 ± 22
	EPAX2	18	44	58	78	96	116
	PHITS	16 ± 1	223 ± 2	292 ± 3	376 ± 5	450 ± 11	588 ± 20
1	This work	19 ± 14	72 ± 5	123 ± 17	239 ± 17	275 ± 13	408 ± 26
	EPAX2	15	35	47	63	78	94
	PHITS	8 ± 1	137 ± 1	259 ± 3	405 ± 5	585 ± 12	792 ± 23
Pedestals	This work	0 ± 4	10 ± 5	67 ± 6	214 ± 17	391 ± 17	718 ± 18
	PHITS	0 ± 1	57 ± 1	129 ± 2	333 ± 5	559 ± 12	900 ± 25
All He	This work	126 ± 15	593 ± 86	705 ± 109	962 ± 139	1126 ± 160	1373 ± 176
	NUCFRG	222	176	192	217	244	271
σ(He)/σ_{cc}	This work	0.79 ± 0.09	0.83 ± 0.12	0.70 ± 0.11	0.62 ± 0.09	0.55 ± 0.08	0.50 ± 0.05
Li	This work	15 ± 3	71 ± 12	85 ± 14	115 ± 19	135 ± 23	165 ± 27
(estimated)	NUCFRG	26	90	102	118	135	151
	EPAX2	16	40	53	71	87	106

TABLE VIII: For the 400 MeV/nucleon beam, fragment cross sections as measured with an acceptance angle of 3.9°.

Z_{eff}		H target	C target	Al target	Cu target	Sn target	Pb target
5	This work	42 ± 5	111 ± 4	133 ± 5	166 ± 3	194 ± 11	232 ± 10
	PHITS	75 ± 1	70 ± 1	78 ± 1	87 ± 2	95 ± 5	133 ± 10
4.4	This work	6 ± 1	10 ± 1	12 ± 2	16 ± 2	22 ± 3	24 ± 3
(Be+He)	PHITS	1 ± 1	5 ± 1	5 ± 1	6± 1	8 ± 1	11 ± 3
4.0	This work	9 ± 1	33 ± 3	40 ± 4	48 ± 5	57 ± 6	65 ± 11
(Be only)	PHITS	15 ± 1	24 ± 1	28 ± 1	27 ± 2	35 ± 3	41 ± 5
Leading Be	This work	15 ± 2	43 ± 2	40 ± 3	48 ± 4	79 ± 5	65 ± 11
(sum)	PHITS	17 ± 1	29 ± 1	33 ± 1	32 ± 2	42 ± 3	52 ± 6
3.5 (3 He or	This work	15 ± 2	47 ± 5	55 ± 6	69 ± 5	80 ± 7	85 ± 14
Li+He)	PHITS	7 ± 1	33 ± 1	54 ± 1	69 ± 2	78 ± 5	88 ± 8
≈ 3 (2 He	This work	22 ± 4	145 ± 5	168 ± 6	210 ± 8	244 ± 9	266 ± 13
or 1 Li)	PHITS	17 ± 1	96 ± 1	49 ± 1	50 ± 2	60 ± 4	71 ± 7
≈ 2	This work	44 ± 4	153 ± 4	192 ± 8	256 ± 4	295 ± 7	363 ± 9
	PHITS	22 ± 1	200 ± 2	258 ± 3	329 ± 5	408 ± 10	508 ± 19
1	This work	20 ± 3	85 ± 6	119 ± 10	182 ± 8	223 ± 14	289 ± 14
	PHITS	6 ± 1	120 ± 1	192 ± 2	262 ± 4	341 ± 9	463 ± 18
Pedestals	This work	2 ± 4	110 ± 11	256 ± 3	549 ± 16	833 ± 12	1303 ± 11
	PHITS	6 ± 1	134 ± 1	367 ± 3	752 ± 7	1137 ± 17	1633 ± 33

TABLE IX: For the 400 MeV/nucleon beam, fragment cross sections as measured with an acceptance angle of 2.5°.

Z_{eff}		H target	C target	Al target	Cu target	Sn target	Pb target
5	This work	41 ± 6	107 ± 3	130 ± 4	155 ± 4	181 ± 10	207 ± 15
	PHITS	75 ± 1	49 ± 1	42 ± 1	41 ± 2	54 ± 4	75 ± 7
4.4	This work	4 ± 1	6 ± 1	7 ± 2	9 ± 4	14 ± 4	6 ± 2
(Be+He)	PHITS	1 ± 1	2 ± 1	1 ± 1	1 ± 1	1 ± 1	3 ± 1
4.0	This work	10 ± 2	31 ± 3	39 ± 4	48 ± 5	55 ± 6	65 ± 8
(Be only)	PHITS	15 ± 1	15 ± 1	15 ± 1	13 ± 1	17 ± 2	26 ± 4
Leading Be	This work	13 ± 2	37 ± 2	46 ± 4	57 ± 6	69 ± 8	71 ± 8
(sum)	PHITS	16 ± 1	16 ± 1	15 ± 1	13 ± 1	17 ± 2	28 ± 4
3.5 (3 He or	This work	13 ± 2	29 ± 3	33 ± 5	38 ± 4	55 ± 9	44 ± 9
Li+He)	PHITS	5 ± 1	11 ± 1	10 ± 1	10 ± 1	15 ± 2	20 ± 4
≈ 3 (2 He	This work	13 ± 3	104 ± 6	118 ± 4	144 ± 10	165 ± 11	170 ± 12
or 1 Li)	PHITS	11 ± 1	21 ± 1	19 ± 1	70 ± 2	19 ± 2	101 ± 8
≈ 2	This work	32 ± 4	142 ± 4	160 ± 4	207 ± 4	241 ± 17	283 ± 7
	PHITS	23 ± 1	152 ± 1	186 ± 2	175 ± 3	273 ± 8	277 ± 14
1	This work	24 ± 2	77 ± 9	100 ± 4	145 ± 5	163 ± 6	187 ± 12
	PHITS	5 ± 1	88 ± 1	123 ± 2	160 ± 3	205 ± 7	267 ± 13
Pedestals	This work	3 ± 5	215 ± 12	407 ± 7	772 ± 17	1123 ± 10	1691 ± 12
	PHITS	15 ± 1	344 ± 2	638 ± 4	1111 ± 9	1578 ± 20	2179 ± 38

Z's in Table 10. Another aspect of these shifts is seen in the relatively large ratios seen for the Z = 2 and Z ≈ 3 categories; these are depopulated by particles leaving the acceptance, but repopulated by feed-down from other categories (e.g., one or two He fragments are outside the 2.5° acceptance, but two or one remain inside). Similarly the Be-only category at small acceptance is repopulated by events with Be + He at large acceptance with the He fragment at an angle greater than 2.5°; the results for Sn and especially Pb targets illustrate this point clearly.

C. Angular Distributions of B and Be Fragments

As discussed above, Goldhaber's statistical model of fragmentation [12], predicts that fragment angular distributions obey Gaussian statistics and broaden as the number of nucleons removed from the primary ion increases. Even at the modest energies considered here, angular distributions of fragments with masses close to that of the primary are strongly forward-peaked. Using the modification of Goldhaber's model presented by Tripathi and Townsend [28], a straightforward calculation shows that the widths of the Gaussians for A_{frag} = 11 and A_{frag} = 10 are about 1.0° and 1.4°, respectively. Considering that the acceptance angle of d3mm2 is greater than 7°, it

TABLE X: Ratios of cross sections measured at the smallest acceptance angle, 2.5° to those measured at the largest acceptance, 7.3°. The beam energy in MeV/nucleon is given in the second column from the left.

	Beam E	C	Al	Cu	Sn	Pb
Z = 5	290	0.92± 0.05	0.86± 0.04	0.86± 0.02	0.83± 0.09	0.79± 0.03
	400	0.96± 0.05	0.97± 0.05	0.91± 0.03	0.87± 0.06	0.83± 0.06
Be+ He	290	0.50± 0.20	0.21± 0.06	0.35± 0.11	0.27± 0.12	0.21± 0.13
	400	0.50± 0.12	0.54± 0.16	0.45± 0.21	0.61± 0.19	0.19± 0.07
Be (sum)	290	0.69± 0.07	0.68± 0.08	0.62± 0.08	0.67± 0.10	0.65± 0.09
	400	0.80± 0.06	0.84± 0.10	0.75± 0.10	0.80± 0.11	0.71± 0.10
Z ≈ 3.5	290	0.28± 0.04	0.36± 0.06	0.27± 0.05	0.27± 0.06	0.18± 0.07
	400	0.37± 0.07	0.40± 0.06	0.35± 0.04	0.45± 0.09	0.28± 0.03
Z ≈ 3	290	0.45± 0.02	0.52± 0.06	0.40± 0.02	0.39± 0.03	0.40± 0.03
	400	0.61± 0.04	0.54± 0.03	0.52± 0.04	0.52± 0.04	0.48± 0.05
Z = 2	290	0.70± 0.03	0.59± 0.07	0.59± 0.06	0.59± 0.14	0.55± 0.08
	400	0.81± 0.05	0.71± 0.04	0.61± 0.02	0.58± 0.05	0.55± 0.03
Z = 1	290	1.07± 0.07	1.01± 0.10	0.73± 0.16	0.44± 0.10	0.58± 0.15
	400	1.07± 0.15	0.81± 0.12	0.61± 0.05	0.59± 0.04	0.46± 0.04
Pedestals	290	7.7 ± 0.8	3.8 ± 0.4	2.6 ± 0.3	2.8 ± 0.4	2.1 ± 0.2
	400	22 ± 11	6.1 ± 0.6	3.6 ± 0.3	2.9 ± 0.1	2.4 ± 0.1

is clear that essentially 100% of the B fragments will be detected in the d3mm1,2 analysis. Similarly, our acceptance model (which includes Coulomb multiple scattering in the target and assumes a point beam) predicts that over 96% of Be (A_{frag}=7, 9) and 93% of Li (A_{frag}=6, 7) fragments will also be detected in d3mm2, even in the worst case (290 MeV/nucleon beam on a 7.2 g cm^{-2} Pb target). Put another way, the efficiency ε, or acceptance fraction, for detecting a particular fragment isotope depends (in the Goldhaber model) on the width of the angular distribution and the acceptance angle as follows:

$$\varepsilon\left(\theta_{acc}\right) = \frac{\int_0^{\theta_{acc}} e^{-\theta^2/2\sigma_\theta^2} d\theta}{\int_0^{\pi} e^{-\theta^2/2\sigma_\vartheta^2} d\theta} \qquad (4)$$

where θ_{acc} is the acceptance angle of a particular detector. (The trivial integration over ϕ has already been carried out, and - in a step justified by the strong forward-peaking of the distributions - the small-angle approximation has been made, i.e., $sin(\theta) \approx \theta$ and $cos(\theta) \approx 1$.) If the beam were truly point-like, and ignoring Coulomb scattering in the target, the widths of the Gaussians would determine the acceptances. That is a good approximation in almost all cases considered here, but in a few instances, Coulomb scattering is significant.

Fragment production cross sections at different acceptance angles, without acceptance corrections, are an indirect measure of the detection efficiency ε as a function of Z and A, as defined by equation 3 above. This, in turn, can provide a measure of σ_0. There are complications, however, that introduce significant uncertainties, which were encountered in the discussion above (Sections IV.B and V) regarding multiple-fragment events. First, we do not identify isotopes, so that a measured ε for a given species is a weighted average over isotopes. Second, the systematic and statistical errors from the measurements can be significant. This is particularly true for B fragments, where ε is close to 1, even in the d3mm5,6 analysis. More direct measurements of σ_0 can be obtained with off-axis experiments if they are designed correctly; the data presented above strongly suggest that accurate measurements of the angular distributions for B and Be would require data points at very small forward angles (less than 5°), and that long runs would required to obtain sufficient statistics.

Bearing these caveats in mind, we can compare the observed fall-off of the measured B and Be cross sections in going from the 7.3° acceptance to 2.5°. Since fragments from the 290 MeV/nucleon beam are less forward-boosted, we confine this analysis to those data. Earlier, we found the multiple-fragment events (as seen in 400 MeV/nucleon data) to be most compatible with a σ_0 of 110-120 MeV/c, somewhat higher than our initially assumed value of 90 ± 10 MeV/c. As a matter of internal consistency, it is important to check whether the small-acceptance results support this larger value. From Table 10, for B fragments, the relevant ratios are 0.92 ± 0.05, 0.86 ± 0.04, 0.86 ± 0.02, 0.83 ± 0.09, and 0.79 ± 0.03 for C, Al, Cu, Sn, and Pb targets, respectively. One can readily see a trend towards smaller ratios with increasing target mass, due to either (or both) increased Coulomb scattering in the target, or the increased Coulomb force at work in the interaction, as explicitly spelled out by Tripathi and Townsend [28]. In our acceptance model, we consider two B isotopes, masses 10 and 11. Even at 2.5°, there are significant differences in acceptance between the two. Considering first the carbon target, where Coulomb scattering in the target is small compared to the nuclear contribution to the angular distribution width, the model predicts acceptances of 0.99 and 0.95 for ^{11}B and ^{10}B, respectively, with σ_0=90 MeV/c. Both of the predicted

values are larger than the observed ratio of 0.92 ± 0.05. Increasing σ_0 to 120 MeV/c, the predicted acceptances drop to 0.97 and 0.86 for the two isotopes, bracketing the measurement. Note that the uncertainty is so large that the measurement can be said to accommodate any possible mixture of the two isotopes, from 100% mass 11 to 100% mass 10. We can construct a χ^2 to serve as a summary statistic, defined as follows:

$$\chi^2 = \sum \frac{\left(R_i - f_i^{calc}\right)^2}{\sigma_i^2} \tag{5}$$

where R_i is the ratio of cross sections as per Table 10, σ_i is the uncertainty in the measurement, f_i^{calc} is the acceptance fraction from our simple model, and the sum runs over all targets from carbon to lead. Six separate calculations are performed for each target, testing the permutations of σ_0 values (90 and 120 MeV/c) and fragment mass number (10, 11, or an equal mixture of the two, which is approximately what NUCFRG2 predicts). By far the smallest χ^2 (2.1 for 5 degrees of freedom) is found for σ_0 = 120 MeV/c and the equal mix of mass 10 and 11 fragments. The next smallest χ^2 is for σ_0 = 120 MeV/c and mass 10 (5.4 for 5 d.o.f.). This result is entirely consistent with the σ_0 inferred from the multiple-fragment event analysis at the higher beam energy presented above.

Repeating the above analysis for charge 4 as per Table 10, using isotopes 7 and 9 and also an equal mixture of the two, the lowest value of χ^2 (= 0.2) is found for the mixture with σ_0 = 120 MeV/c. Other values of χ^2 that are less than 1 per degree of freedom are found for mass 9 and σ_0 = 120 MeV/c (χ^2 = 3.6) and mass 7 with σ_0=90 MeV/c (χ^2 = 0.8). NUCFRG2 predicts that about half of the Be fragments should be mass 7, the other half heavier (mostly mass 9). EPAX2 predicts slightly more mass 9 than mass 7, with about half of the Be cross section going into (unobservable) ^{8}Be. Therefore, although a numerically acceptable solution with σ_0=90 MeV/c was found, it is not very plausible. The most plausible solution would seem to be the mixture, with σ_0 = 120 MeV/c.

In summary, the B and Be cross sections at small acceptance provide a useful cross-check of the acceptance calculations performed in attempting to disentangle the multiple-fragment events. The results obtained with the 290 MeV/nucleon beam are more sensitive to variations in angular distributions, but lead to the same conclusion as the multiple-fragment analysis done using 400 MeV/nucleon data, namely, that σ_0 must be about 120 MeV/c in order for our acceptance model to match the data. Reasonable mixtures of B and Be isotopes, along with this relatively large value of σ_0, yield the smallest χ^2 values.

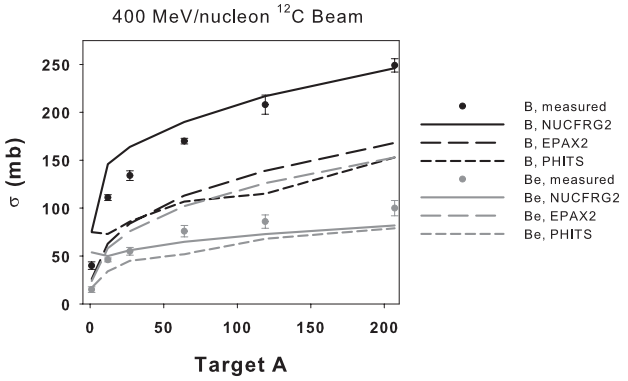

FIG. 14: Fragment cross sections for B (black data points and model curves) and Be (blue), plotted against target mass number, for the 400 MeV/nucleon beam. The models all do poorly for the hydrogen target. NUCFRG2 comes reasonably close to reproducing the data for other targets, but PHITS and EPAX2 predictions are much less accurate.

D. B and Be Fragment Cross Sections Compared to Models

In Figure 14, we show the measured large-acceptance cross sections for B and Be production on all targets, obtained with the 400 MeV/nucleon beam. Also shown are curves for NUCFRG2, EPAX2, and PHITS. We restrict the comparison to these two fragment species since there are no particle identification ambiguities associated with either. For both B and Be, NUCFRG2 comes closest to the data points, particularly for large target A, but it is not close for either cross section for the hydrogen-target, nor for B for the C, Al, and Cu targets. For B, the EPAX2 and PHITS predictions are far below the measured cross sections. PHITS is also well below the data for Be, while EPAX2 is well above.

In general, the models are furthest from the data for the H target. In Table 11, we show the ratios of predicted to measured cross sections for B and Be fragments for the three models. Results for the H target are shown separately from the average values obtained with the other targets. We note that NUCFRG2 predicts a larger cross section for C + H → Be + X than for C + C → Be + X. Similarly, PHITS predicts a larger cross section for C + H → B + X than for C + C → B + X. Both are unphysical, and neither agrees with the data. For targets other than H, on average NUCFRG2 is in good agreement with the data, while EPAX2 and PHITS are not.

E. Large-Acceptance Light Fragment Cross Sections Compared to Models

In Tables 4 and 7, NUCFRG2 and EPAX2 predictions are shown with our estimates of Li cross sections, in the bottom sections of each table. For hydrogen targets, EPAX2 agrees well with the estimates, but for other tar-

TABLE XI: Ratios of calculated B and Be fragment cross sections to measured cross sections, for hydrogen targets and all others.

Model	Model/Data, B fragments, H target	Model/Data, B fragments, All targets but H	Model/Data, Be fragments, H target	Model/Data, Be fragments, All targets but H
NUCFRG2	1.90	1.14	3.60	0.93
EPAX2	0.65	0.64	1.60	1.40
PHITS	1.88	0.62	1.13	0.76

gets, the estimated cross sections are considerably higher than EPAX2 predicts. The EPAX2 cross sections are, for C through Pb targets, about 60% of the estimated data values. NUCFRG2 cross sections for Li agree well with the measurements for copper and heavier targets, are slightly larger than the C and Al data, and are well above the H-target data. The trend is similar to that seen in Figure 14 in comparing NUCFRG2 to Be cross sections as a function of target mass number, in that the model-predicted values rise less steeply with target mass than do the data.

In comparing the models to He cross sections, we place the NUCFRG2 predictions next to our estimated total He cross sections in the next-to-last section of each table, and both the EPAX2 and PHITS cross sections are placed next to the Z $\approx$ 2 data. The reason for this ordering is that the NUCFRG2 cross sections are multiplicity weighted, while it appears the EPAX2 cross sections are not, and the PHITS simulations allow for a direct comparison in the Z $\approx$ 2 category since the events are reconstructed in analogy with the data. In this category, the EPAX2 cross sections are consistently about 20 to 25% of the measured values, except for the H target data, where the agreement is somewhat better. The PHITS results are in fairly good agreement with the data for C and heavier targets, coming within 10-30% of the data, though in all cases the model predicts larger cross sections than are seen in the data. In the estimates of the total He cross sections, NUCFRG2 is well above the data for H targets, but far below for all other targets.

Since we cannot measure or infer the true multiplicity-weighted cross sections for charge 1 from these data, we have not shown the NUCFRG2 predictions for this category. Cast in terms of multiplicity, NUCFRG2 typically predicts (on average) about 5 protons per interaction, varying slightly with the target. Even though we do not measure anything like the total proton yield, we can say that this prediction is not supported by the data. In the analysis of the off-axis data presented above, it was noted that the total proton yield appears to be, very approximately, about twice the yield of He. Since the average He multiplicities are, from Tables 4 and 7, in all cases less than 1, this would suggest the average proton multiplicity must be less than 2. Thus NUCFRG2 appears to predict far larger yield of protons, and a far smaller yield of He, than is seen in the data. PHITS predictions for the charge 1 category can be meaningfully compared to the data, and are found to be 50-100% larger than the measurements for C and heavier targets. (We do compare to the H target data since the uncertainties are so large.) Finally, EPAX2 predictions are well below the data, as was also the case for Li and He fragments.

In summary, although NUCFRG2 comes reasonably close to the estimated Li cross sections and those measured for B and Be, it disagrees with the data for He and protons. Cross sections predicted by EPAX2 are, with the exceptions of H targets and Be fragments, virtually all smaller than the measured cross sections. PHITS appears to produce too many light fragments, especially He and H, while producing too few Be and B fragments. Thus, none of the models accurately reproduces the measured cross sections across the full range of targets and fragments.

F. Acceptance-Dependent Results Compared to PHITS

The fact that PHITS is a three-dimensional simulation allows us to make comparisons not just at large acceptance (as with NUCFRG2 and EPAX2), but also at small acceptance, and to compare against all the measured cross sections, not just B and Be. Figure 15 shows data and PHITS results for aluminum targets with the 400 MeV/nucleon beam energy at both large (7.3°) and small (2.5°) acceptances. For both, the general shape of the PHITS curves are in reasonable accord with the data, though only a few points (effective charges of 2, 3.5, and 4 at large acceptance) can be said to be in good agreement. At large acceptance, the model cross sections are above the data for $Z_{eff} \leq 2$, and below the data for charges 4 and especially 5. At small acceptance, the discrepancies are much worse, particularly for Z_{eff} from 3 to 5, where the measured cross sections are far greater than those predicted by the simulation. Since the charge-changing cross sections in the model are close to the measurements, the disparity at higher Z must be compensated by a disparity in the other direction at lower Z; this occurs only for pedestals, where the data are some 230 mb below the model. This discrepancy alone accounts for some 23% of the charge-changing cross section.

It appears that PHITS, which incorporates JQMD [29] to simulate the physics of nucleon-nucleon collisions, is not well-tuned for these reactions. Several adjustable parameters appear to be relevant, including the compressibility of the interacting nuclei and the nucleon binding

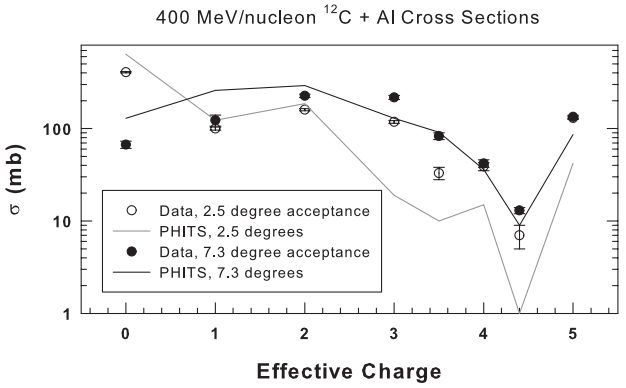

FIG. 15: Comparison of cross sections derived from PHITS for 290 MeV/nucleon carbon on aluminum targets at both large and small acceptance. Although PHITS predicts charge-changing cross sections with reasonable accuracy, the fragment cross sections do not agree well with the data, particularly at small acceptance.

distance chosen in the statistical decay part of the model. It could also be the case that the model is assigning excessive p_T to the fragments, with the result that many of the reconstructed events have non-leading light fragments inside the acceptance cone, presumably with the higher-charge fragments outside the acceptance. Any or all of these could be the cause(s) of the observed discrepancies.

Further insight into these questions can be gained from additional examination of Figure 15 for small acceptance. It can be seen that the discrepancies between the data and model for B and Be fragments are much worse at small acceptance than at large acceptance. This lends support to the notion that the model is assigning excessive p_T to the outgoing fragments, even those in which few nucleons have been removed from the primary carbon. Along the same lines, the number of Z $\approx$ 3.5 events predicted by PHITS at large acceptance agrees well with the data, but is low by a factor of three at small acceptance. However, even at large acceptance, PHITS predictions are (except for the H target) consistently lower than the data for B and Be. This suggests that the problem or problems in PHITS are not limited to excessive p_T transfer.

IX. DISCUSSION

Charge-changing and fragment production cross sections for interactions of ^{12}C ions at 290 MeV/nucleon and 400 MeV/nucleon on several elemental targets have been measured. The charge-changing cross sections agree to within 15% of those predicted by the semiempirical NUCFRG2 model, with better agreement (typically ¡ 10%) seen for the higher-mass targets. The cross sections are within 14% of the simple geometric Bradt-Peters form using parameters determined by Chen *et al.* Adjusting the parameters r_0 (from 1.35 to 1.29) and b (from 0.83 to 0.86), the calculated values are within 3% of the data for all cases except 290 MeV/nucleon beam on Cu, which is within 5%. The PHITS Monte Carlo code was used in the comparison by employing a novel method that combined multiple fragments as single events, as in the experiment. By this method, PHITS predicts the charge-changing cross sections to within 7% (except for 290 MeV/nucleon ^{12}C on hydrogen).

Multiple fragment events, in which two He fragments in coincidence are essentially indistinguishable from a single Li fragment in the silicon detectors, make it difficult to extract information beyond the charge-changing cross sections and the B and Be fragment cross sections. However, by using the NaI counter and off-axis data, we are able to estimate that the He yield is 7 to 10 times larger than the Li yield, and we apply this estimate to obtain (with large uncertainties) the Li and He cross sections, which have not previously been reported in 0° measurements with carbon beams.

Using a simple model of fragment angular distributions, we infer that the parameter that determines the momentum widths in Goldhaber's formulation, σ_0, is in the range 110-120 MeV/c for these interactions. This is on the high side of previously-reported measurements for light fragments, but it is consistent with all aspects of the data. And it may be theoretically allowed when one accounts for dynamical contributions to the transverse momentum widths.

Fragment production cross sections for the large acceptances are, except for H target data, in good agreement with NUCFRG2, but do not agree well with predictions from EPAX2 and PHITS. The PHITS code allows a full three-dimensional simulation of the experiment including acceptance effects, but the small-acceptance data in particular are not well reproduced. The comparisons between PHITS and the data, at both large and small acceptance, suggest that adjustments to a few parameters might yield substantially better agreement. On the whole, the models are not in particularly good agreement with the data, which is surprising in view of the small number of nucleons in the projectile and the relatively low energies. This perhaps indicates a lack of attention by theorists to this domain, which remains relevant to space and medical applications.

Acknowledgments

We gratefully acknowledge the tremendous efforts of the HIMAC accelerator operators, in particular Dr. Eiichi Takada, for providing us with excellent beams and stable conditions in this and other runs. We thank Dr. Hiroshi Iwase of KEK and Mr. Tatsuto Komiyama of JAXA for their valuable help with the PHITS program, and Drs. Koji Niita and Tatsuhiko Saito of JAERI for providing us with the PHITS code. We also thank Ryan Norman of the Worcester Polytechnic Institute

Physics Department for providing the NUCFRG2 cross sections. This work was supported at LBNL by the Space Radiation Health Program of the National Aeronautics and Space Administration under NASA Grant Numbers L14230C and H31909D, through the U.S. Department of Energy under Contract No. DE-AC03076SF00098. At HIMAC, this work was supported in part by the Research Project with Heavy Ions at NIRS-HIMAC, Project No. P037.

[1] K. Noda, T. Fujisawa, T. Furukawa, Y. Iwata, T. Kanai, M. Kanazawa, N. Kanematsu, A. Kitagawa, Y. Kobayashi, M. Komori, et al., in *Proceedings of EPAC 2004, Lucerne, Switzerland* (2004), URL `http://tinyurl.com/2fvdkn`.

[2] U. Amaldi and G. Kraft, Rep. Prog. Phys. **68**, 1861 (2005).

[3] G. D. Badhwar and P. M. O'Neill, Nucl. Tracks Radiat. Meas. **20**, 403 (1992).

[4] *NCRP Report No. 98* (National Council on Radiation Protection and Measurements, 1989), p. 22.

[5] J. W. Wilson, F. A. Cucinotta, M.-H. Y. Kim, and W. Schimmerling, Physica Medica **XCII, Supp. 1**, 1 (2001).

[6] C. Zeitlin, K. Frankel, W. Gong, L. Heilbronn, E. Lampo, R. Leres, J. Miller, and W. Schimmerling, Rad. Meas. **23**, 65 (1994).

[7] C. Zeitlin, J. Miller, L. Heilbronn, K. Frankel, W. Gong, and W. Schimmerling, Rad. Res **154**, 655 (1996).

[8] C. Zeitlin, L. Heilbronn, J. Miller, S. E. Rademacher, T. Borak, T. R. Carter, K. A. Frankel, W. Schimmerling, and C. E. Stronach, Phys. Rev. C **56**, 388 (1997).

[9] C. Zeitlin, A. Fukumura, L. Heilbronn, Y. Iwata, J. Miller, and T. Murakami, Phys. Rev. C **64**, 024902 (2001).

[10] C. L. Tessa, S. Guetersloh, L. Heilbronn, J. Miller, L. Sihver, and C. Zeitlin, Adv. Space Res. **35**, 223 (2005).

[11] C. Zeitlin, A. Fukumura, L. Heilbronn, S. Guetersloh, Y. Iwata, J. Miller, and T. Murakami, Nucl. Phys. A p. 341 (2007).

[12] A. Goldhaber, Phys. Lett. B **53**, 306 (1974).

[13] R. Brun, O. Couet, C. E. Vandoni, and P. Zanarini, Comput. Phys. Commun. **16**, 147 (1989).

[14] J. Pouliot, Y. Chan, D. E. GiGregorio, B. A. Harmon, R. Knop, C. Moisan, R. Roy, and R. G. Stokstad, Phys. Rev. C **43**, 735 (1991).

[15] F. P. Brady, W. B. Christie, J. L. Romero, C. E. Tull, J. L. Chance, G. P. Grim, J. C. Young, H. J. Crawford, T. Kobayashi, P. J. Lindstrom, et al., Phys. Rev. C **50**, R525 (1994).

[16] C. Zeitlin, L. Heilbronn, J. Miller, L. Townsend, and J. W. Wilson, Radiat. Res. **154**, 655 (1996).

[17] J. W. Wilson, J. L. Shinn, L. W. Townsend, R. K. Tripathi, F. F. Badavi, and S. Y. Chun, Nucl. Instrum. Methods Phys. Res. B **94**, 95 (1994).

[18] Y. Iwata, T. Murakami, H. Sato, H. Iwase, T. Nakamura, T. Kurosawa, and L. Heilbronn, Phys. Rev. C **64**, 054609 (2001).

[19] K. Summerer and B. Blank, Phys. Rev. C **61**, 034607 (2000).

[20] H. Iwase, K. Niita, and T. Nakamura, J. Nucl. Sci. Technol. **39**, 1142 (2002).

[21] T. Sato, L. Sihver, H. Iwase, H. Nakashima, and K. Niita, Adv. Space Res. **35**, 208 (2005).

[22] D. Mancusi, L. Sihver, K. Gustafsson, C. L. Tessa, S. Guetersloh, C. Zeitlin, J. Miller, L. Heilbronn, K. Niita, and T. Sato, Nucl. Instrum. Methods Phys. Res. B **254**, 30 (2007).

[23] H. Aiginger, V. Andersen, F. Ballarini, G. Battistoni, M. Campanella, M. Carboni, F. Cerutti, A. Empl, W. Enghardt, A. Fasso, et al., Adv. Space Res. **35**, 214 (2005).

[24] S. Guetersloh, C. Zeitlin, L. Heilbronn, J. Miller, T. Komiyama, A. Fukumura, Y. Iwata, T. Murakami, and M. Bhattacharya, Nucl. Instr. Meth. in Phys. Res. B **252**, 319 (2006).

[25] H. C. Bradt and B. Peters, Phys. Rev. **77**, 54 (1950).

[26] C.-X. Chen, S. Albergo, Z. Caccia, S. Costa, H. J. Crawford, M. Cronqvist, J. Engelage, P. Ferrando, R. Fonte, L. Greiner, et al., Phys. Rev. C **49**, 3200 (1994).

[27] W. Webber, J. Kish, and D. Schrier, Phys. Rev. C **14-2**, 520 (1990).

[28] R. K. Tripathi and L. W. Townsend, Phys. Rev. C **49**, 2237 (1994).

[29] K. Niita, S. Chiba, T. Maruyama, T. Maruyama, H. Takada, T. Fukahori, Y. Nakahara, and A. Iwamoto, Phys. Rev. C **52**, 2620 (1995).